The Meteoritical Society

Meteoritics & Planetary Science 60, Nr 8, 1762–1784 (2025)
doi: 10.1111/maps.70005

Origin of the metal in chondritic and achondritic lithologies of the Sierra Gorda 013 CBa-like chondrite

Marina A. IVANOVA [1]*, Svetlana N. TEPLYAKOVA [1], Cyril A. LORENZ [1], Shuying YANG [2], and Munir HUMAYUN [2]

[1]Vernadsky Institute of Geochemistry and Analytical Chemistry, Moscow, Russia
[2]National High Magnetic Field Laboratory and Department of Earth, Ocean & Atmospheric Science, Florida State University, Tallahassee, Florida, USA

***Correspondence**
Marina A. Ivanova, Vernadsky Institute of Geochemistry and Analytical Chemistry, Moscow 119991, Russia.
Email: meteorite2000@mail.ru

(Received 04 December 2023; revision accepted 02 April 2025)

Abstract–Sierra Gorda 013 (SG 013) is an unusual CBa-like chondrite containing two texturally different, isotopically identical lithologies—chondritic (L1) and achondritic (L2), which should have a common origin. The metal globules of the L1 metal preserved the magmatic pattern of the siderophile element distribution that indicates they had a fractionated precursor. In this work, the trace element metal composition of lithology 2 was studied, and the revisited LA-ICP-MS data on the L1 metal was presented. Lithologies 1 and 2 have Ni and Co in the range of CB chondrites. The Ni-Co distribution in L1 and depletion in Cr of both lithologies with a negative Cr-Ni correlation are similar to that of the magmatic irons. Highly refractory siderophile element (HRSE) (W, Re, Os, Ir, Pt, Ru, Rh, and Mo) compositions of the L1 metal are highly fractionated relative to CI, but the L2 metal has a nearly uniform HRSE distribution similar to the depleted patterns of some HRSE-poor L1 metal compositions. Metal from both lithologies is depleted in volatile siderophile elements. In the L1 metal globules, the metal composition shows definite linear correlations of the HRSE elements versus Ni similar to those observed in many magmatic iron meteorites, distinct from those of the CH/CBb-zoned metal. Meanwhile, the L2 metal compositions are systematically plotted as limited clusters in the middle of the L1 trends. Based on a fractional crystallization (FC) model of the CR-like metal composition, it was shown that the distribution of siderophile elements in the metal globules of L1 can cover the full range of the fractional crystallization products of a metallic (Fe-Ni-S) liquid from the core of a differentiated body at S content 13 wt%. In contrast, the metal from L2 corresponds to a more limited range of fractional crystallization products and indicates a mixture of the fractionated metal with the primitive metal from the chondritic colliding body. Our results suggest that during a catastrophic impact event when the metallic core of a differentiated body was disrupted, the L1 lithology was quickly cooled in the impact plume, more reduced than that of CB chondrites and avoided equilibration with plume gas and preserved its fractionated HRSE patterns. The distribution of siderophile volatile elements and Au was likely overprinted by high-temperature processes of volatilization and recondensation to different degrees in the impact plume under disequilibrium conditions. The L2 metal probably avoided equilibration with the plume gas and was affected by thermal metamorphism up to 900°C in the SG 013 parent body, which possibly resulted in the higher W abundance compared to the L1 metal with a magmatic Ir-W trend due to the redox reactions with silicates under reducing conditions.

INTRODUCTION

The metal-rich carbonaceous chondrites (CR, CH, and CB) are very intriguing among other groups of chondrites. The CH and CB groups of chondrites are texturally and mineralogically very diverse but genetically related by oxygen isotope compositions and the origin of some components like zoned Fe,Ni-metal, and Ca,Al-rich inclusions in CH/CBb chondrites (e.g., Krot et al., 2002, 2008, 2012, 2022; van Kooten et al., 2016; Weisberg et al., 1995, 2001; Weyrauch et al., 2021). The CH/CBb chondrite Isheyevo (Ivanova et al., 2008) combines characteristics of both groups. These meteorites were formed in the same protoplanetary disk reservoir based on oxygen isotopes and nucleosynthetic isotope data (van Kooten et al., 2016), 3.8 ± 0.8 Ma (Wölfer et al., 2023) after the formation of the Ca-Al-rich inclusions (Connelly et al., 2012).

The CB (Bencubbin-like) metal-rich carbonaceous chondrites are subdivided into the CBa and CBb subgroups (Krot et al., 2002; Weisberg et al., 2001). The CBa chondrites are composed predominantly of ~centimeter-sized skeletal olivine chondrules and unzoned Fe,Ni-metal-troilite nodules (e.g., Campbell et al., 2002; Weisberg et al., 1995, 2001; Weisberg & Kimura, 2010; and references therein). The CBb chondrites are finer grained than the CBa chondrites and consist of chemically zoned and unzoned Fe,Ni-metal grains, Fe,Ni-metal-troilite nodules, cryptocrystalline and skeletal olivine (SO) chondrules, and rare refractory inclusions (e.g., Campbell et al., 2001; Krot et al., 2002, 2008, 2012, 2021; Weisberg et al., 2001, and references therein). Both subgroups contain exceptionally rare porphyritic chondrules and no fine-grained matrix between interchondrule space.

In previous studies, it was concluded that CB chondrites could have formed by a sequence of nebular processes (e.g., Campbell et al., 2001, 2005; Krot et al., 2002; Meibom et al., 1999; Newsom & Drake, 1979; Weisberg et al., 1990, 2001). Alternatively, it was proposed that CBs formed from a giant collision of protoplanets producing an impact plume (e.g., Campbell et al., 2002; Fedkin et al., 2015; Florin et al., 2021; Kallemeyn et al., 1978; Koefoed et al., 2022; Krot et al., 2005, 2022; Lorenz et al., 2023; Oulton et al., 2016; Petaev et al., 2001; Wasson & Kallemeyn, 1990; Weyrauch et al., 2019). Isotopic investigations of ^{56}Fe, ^{60}Ni, and trace element studies in zoned and unzoned CB metal (Koefoed et al., 2022; Weyrauch et al., 2019) support their formation in an impact plume. The distribution of siderophile elements and their isotopes indicates turbulent gas mixing, including the movement of metal particles during their formation, between inner and outer regions of the impact plume, indicating elevated oxygen fugacity in the gas reservoir (Weyrauch et al., 2019, 2021).

In addition to typical CBa and CBb chondrites, two metal-rich carbonaceous chondrites with anomalous characteristics have been described recently—Fountain Hills (FH) (Krot et al., 2023; Lauretta et al., 2004, 2009; Weisberg & Ebel, 2009) and Sierra Gorda 013 (SG 013) (Hoffman, 2021; Ivanova et al., 2019, 2022; Krot et al., 2023). They have CB-like bulk O-isotope compositions, but in addition to SO chondrules, they contain barred olivine (BO) chondrules and coarse-grained igneous clasts/porphyritic chondrule-like objects composed of olivine, low-Ca-pyroxene, and minor plagioclase, and high-Ca pyroxene.

SG 013 is a unique CBa-like chondrite and very different from all known CB chondrites since it contains two texturally different but genetically linked lithologies (Ivanova et al., 2022). Lithology 1 (L1) contains Fe, Ni-metal (~80 vol%) represented by large globules up to 0.6 cm in size (Figure 1a), smaller metallic particles, and ~20 vol% of chondrule-like POP, BO, and SO clasts (up to 5 mm in diameter). The globules mostly consist of low-Ni metal kamacite and small, rare grains of high-Ni taenite and schreibersite. Chromite occurs along the boundary of metal globules and chondrules (Hoffman, 2021; Ivanova et al., 2022) and inside the metal globules (Lorenz et al., 2023). Lithology 2 (L2) is a crystalline rock crosscut by fractures filled by terrestrial iron hydroxide (Figure 1b). It has a lower abundance of Fe,Ni-metal (~25 vol%) than L1. Metal occurs as particles up to 1 mm in size and irregular shape, between evenly distributed coarse-grained minerals (~75 vol%): olivine, pyroxene, anorthite, chromite, and schreibersite (Ivanova et al., 2022). Small grains of schreibersite and high-Ni taenite were found in association with Ni-poor kamacite grains (Figure 2). Schreibersite was also found in a contact of the metal particles (Figure 3). Unlike L1, L2 contains only rare tiny grains of sulfides in veins, most of which were probably oxidized by terrestrial weathering.

Bulk major and trace element geochemistry of chondrules and bulk siderophile compositions in metal globules of L1 record elemental fractionation during metal-silicate equilibration on a differentiated body, overprinted by evaporative loss of volatiles in the impact melt plume. The REE distribution of L1 chondrules has a signature corresponding to possible differentiated precursor material. In contrast to L1, the REE patterns of the L2 silicates closely match the CI chondrite composition (Ivanova et al., 2022). Thus, the formation of SG 013 could be explained by collisions of chondritic and differentiated planetesimals and subsequent processing in the resulting impact plume (Ivanova et al., 2022; Koefoed et al., 2022; Oulton et al., 2016).

Lorenz et al. (2023) showed heterogeneous physicochemical conditions in the impact plume based on the study of glassy inclusions enclosed in the metal

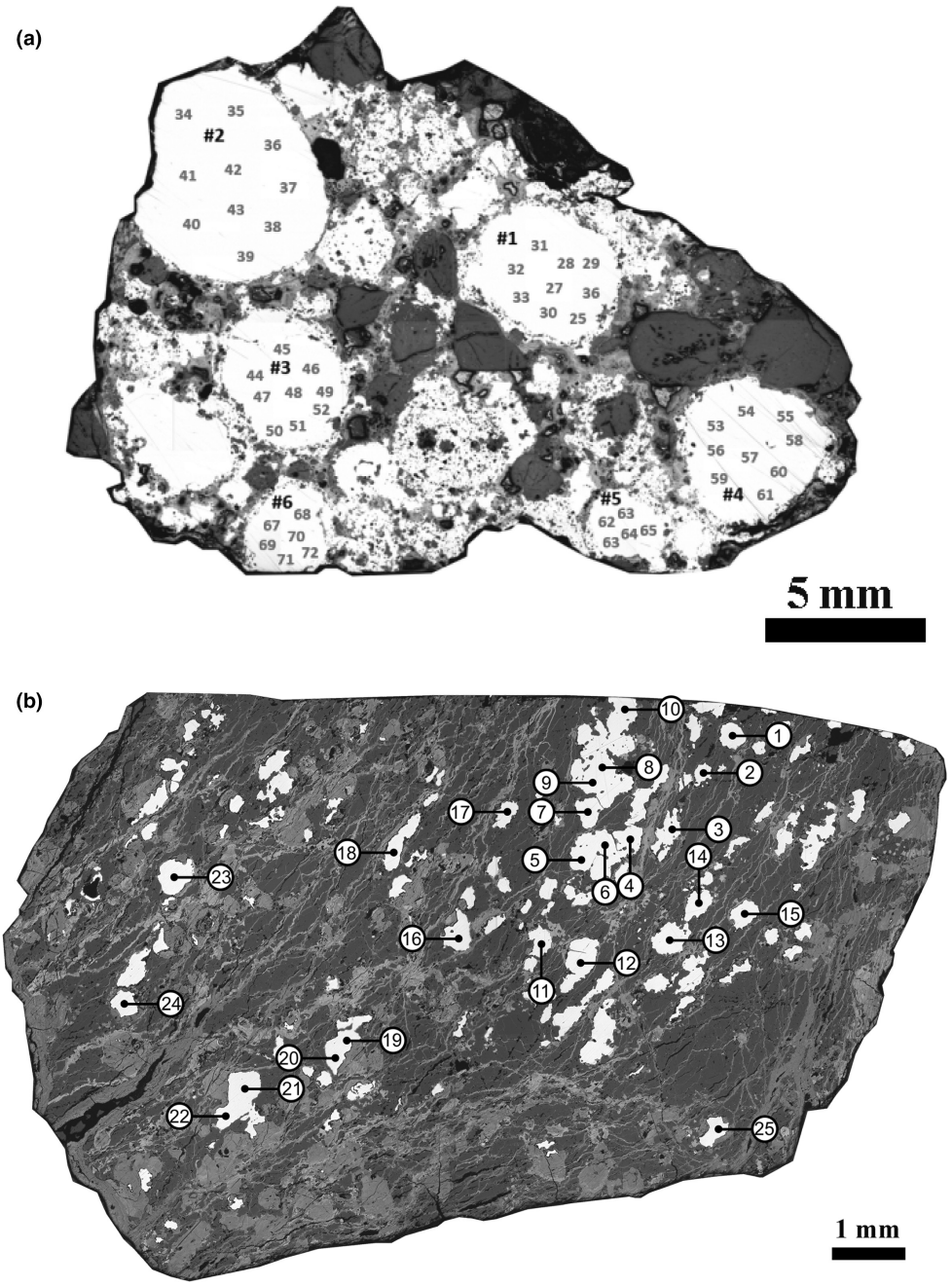

FIGURE 1. Locations of the LA-ICP-MS spot analyses of SG 013: (a) in metal globules from lithology (L1). (b) Spot locations in metal particles from lithology (L2).

globules of L1. The same conclusion was made by Krot et al. (2023) which showed that magnesian nonporphyritic (barred olivine, skeletal olivine, and cryptocrystalline) chondrules in the CBas, CBbs, and porphyritic chondrule-like objects in L1 of SG 013 and in Fountain Hills formed in different zones of the CB impact plume characterized by variable pressure, temperature, cooling rates, and redox conditions. It was also proposed by Krot et al. (2023) that L2 possibly represents fragments of one of the colliding bodies and therefore one of the CB chondrule precursors. However, both lithologies have similar oxygen isotopic compositions, indicating a similar cosmochemical reservoir of the bodies' formation, and do not allow to distinguish them.

The metal composition in L2 could be another indicator of the nature of the origin of lithology and the

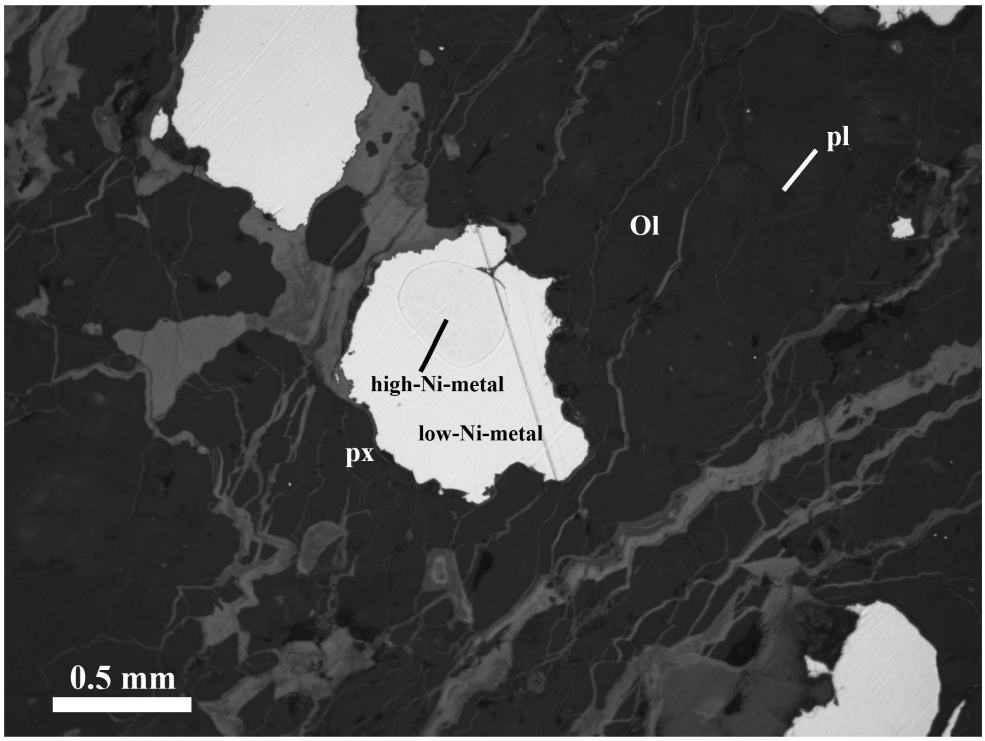

FIGURE 2. BSE image of the Ni-poor metal particle containing schreibersite from achondritic lithology 2 of SG 013.

whole SG 013 meteorite. However, the trace element composition L2 metal has not previously been studied. Here, we present new LA-ICP-MS results on measurements of major and trace elements in the metal particles of lithology 2 to compare the trace element distribution patterns in the L1 and L2 lithologies. For this, we revisit our previous LA-ICP-MS data obtained for the metal globules from the chondritic L1 lithology of SG 013 in Ivanova et al. (2022). We also compare the major and trace element geochemistry of metal from both lithologies with that of typical CH-CB chondrites, zoned CH/CBb metal and iron meteorites of different groups to understand the evolution of the SG 013 metal.

ANALYTICAL PROCEDURE

Laser Ablation ICP-MS Analysis of Elemental Abundance

One polished section of total surface area ~2 cm^2 of the SG 013 achondritic lithology (L2) was studied by a high-resolution Thermo Finnigan Element XR™ ICP-MS equipped with an Elemental Scientific Lasers (ESL) New Wave™ UP-193FX ArF (193 nm) excimer laser ablation system at the Plasma Analytical Facility of the National High Magnetic Field Laboratory, Florida State University (Campbell & Humayun, 1999; Humayun, 2012; Yang et al., 2018). Metal globules from SG 013 L1 were ablated using 150-μm spot sizes, and metal particles from L2 were ablated using 100 μm spot sizes, at a 50 Hz repetition rate for 20 s per spot (Figure 1a,b). The mass peaks acquired were ^{31}P, ^{34}S, ^{47}Ti, ^{51}V, ^{53}Cr, ^{57}Fe, ^{59}Co, ^{60}Ni, ^{63}Cu, ^{66}Zn, ^{69}Ga, ^{75}As, ^{95}Mo, ^{102}Ru, ^{103}Rh, ^{106}Pd, ^{120}Sn, ^{121}Sb, ^{182}W, ^{185}Re, ^{190}Os, ^{193}Ir, ^{195}Pt, and ^{197}Au. The standards used in this study included Hoba IVB (Ru, Rh, Pd, Re, Os, Ir, and Pt; Walker et al., 2008), North Chile (Filomena IIA) (Cu, Ga, Ge, As, W, and Au; Wasson et al., 1989), NIST SRM 1263a steel (V, Cr, Cu, As, Mo, Ag, Sb, W, and Au; Campbell et al., 2002), and NIST SRM 610 silicate glass (Si, P, S; Jochum et al., 2006). Precision of the data depends on spot size, concentration in the target, the isotopic abundance of the peak monitored, and the intensity of isobaric interferences and backgrounds. To assess precision, we show data for five replicate analyses of three metal standards representing a range of compositions using the same spot size used on the SG 013 metals and estimated reproducibility (Table S1). Each chemical composition in Tables 1 and 2 represents the result of one ICP analysis of one laser spot in the L1 and L2 metals. The large metal globules contain several analyzed spots.

RESULTS

LA-ICP-MS data for the metal globules of L1 and metal particles of L2 are presented in Tables 1 and 2. The metal particles used for measurements do not contain any

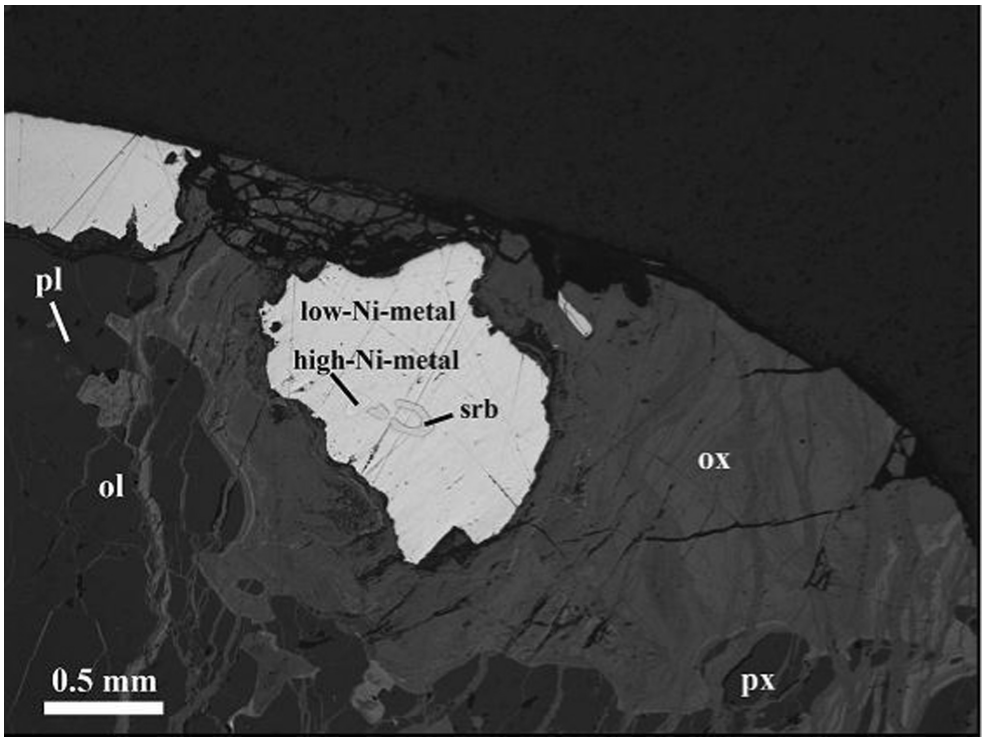

FIGURE 3. BSE image of Ni-poor Fe,Ni-metal particles from lithology 2 of SG 013. It contains schreibersite and taenite (high-Ni)-metal.

inclusions of silicates nor fractures filled by weathering products.

Major Element Composition of the SG 013 Metal

The Ni and Co compositions of the L1 metal globules shown on Figure 4a form a weakly positively inclined cluster elongated on the Ni axis. It is crossing the CI line and is localized on the high-Co end of the CR field (Kong et al., 1999; Kong & Palme, 1999; van Kooten et al., 2022) and the unzoned CH-CB metal field (Campbell et al., 2002), different from the CBb zoned metal trend (Campbell et al., 2001; Weyrauch et al., 2019) (Figure 4b). The pattern of Ni and Co distribution of the L1 metal has a similar configuration to the magmatic iron meteorite groups patterns (Scott, 1972; Scott & Wasson, 1975; Wasson, 1999; Wasson et al., 2007; Wasson & Richardson, 2001).

The Co-Ni distribution in the L2 metal has a slightly negative trend (Figure 4a) which may indicate a heterogeneous mixing of taenite and kamacite in the metal composition acquired by the LA-ICP-MS measurements. The average Ni content in the L2 metal (7.09 ± 0.22 wt%) is higher than in the L1 metal (6.48 ± 0.22 wt%), and the average Co content is similar in the metal from both lithologies (3233 ± 36 ppm in L1 and 3157 ± 144 ppm in L2) (Table 2).

All L1 metal is depleted in Cr, in contrast to the CB and CR chondrite metal (Campbell et al., 2001; Wasson & Rubin, 2010). L1's Cr-Ni distribution is similar to that of iron meteorites of IIAB, IIIAB, and IVA chemical groups (Wasson, 1999; Wasson & Richardson, 2001) (Figure 5). The L2 metal as well as L1 metal is depleted in Cr relative to CI and have similar Cr-Ni distribution defining a group in between IIAB and IIIAB and with a very similar slope (Figure 5). The average Cr content in L2 metal is 0.012 ± 0.008 wt%, similar to L1.

Trace Element Composition of the SG 013 Metal

The major and trace element distributions of the L1 and L2 metal normalized to Ni and CI chondrites are shown in Figure 6a. As reported in Ivanova et al. (2022), the L1 metal had highly refractory siderophile elements (HRSE)-rich and HRSE-poor compositions indicating significant fractionation. The elements include W, Re, Os, Ir, Pt, Ru, Rh, and Mo. The L1 metal is enriched in Pd and depleted in Au, and it is depleted in volatile siderophile elements (VSE) such as Sb, As, and Ga relative to CI composition. The L2 metal is strongly depleted in HRSE and VSE, similar to the HRSE-poor compositions of the L1 metal (Figure 6a). The L2 metal is also depleted in Pd and Au. Each large metal globule of the L1 metal can simultaneously contain metal compositions of the L1

TABLE 1. Major and trace element abundances in metal of the Sierra Gorda 013 lithology 1 (ppm).

	D. L.	56	57	59	60	61	48	49	50	51
P	*3*	1613	1493	1696	1629	1784	1693	1845	1837	1648
S	*37*	894	919	1267	899	932	802	778	720	556
Ti	*3*	22.8	19.5	23.3	21.5	17.3	29.5	24.1	23.7	21.9
V	*0.02*	0.19	0.20	0.28	0.17	0.31	0.50	0.28	0.47	0.36
Cr	*0.7*	102	110	408	122	128	70.9	77.7	63.1	72.5
Fe	*1*	934,000	933,000	933,000	934,000	934,000	932,000	935,000	933,000	933,000
Co	*0.1*	3220	3240	3250	3250	3220	3200	3270	3170	3190
Ni	*0.2*	63,000	64,000	63,000	63,000	62,500	64,500	61,300	63,500	64,100
Cu	*0.03*	42.1	44.2	42.9	41.0	40.8	43.5	41.2	42.2	43.3
Zn	*0.02*	0.18	0.19	0.24	0.32	0.32	0.18	0.24	0.27	0.32
Ga	*0.02*	1.82	2.25	1.96	1.90	1.79	1.93	1.91	2.09	1.91
As	*0.07*	3.29	3.25	3.49	3.47	3.68	3.47	3.67	3.47	3.32
Mo	*0.2*	10.5	8.15	10.8	11.9	14.4	10.6	11.0	9.70	6.85
Ru	*0.03*	7.23	5.64	7.22	7.84	9.15	7.03	6.18	6.08	5.20
Rh	*0.02*	2.04	1.70	1.90	2.06	2.28	1.81	1.95	1.89	1.56
Pd	*0.02*	4.36	4.37	4.67	4.63	4.76	4.30	4.24	4.38	3.78
Sb	*0.02*	0.07	0.09	0.09	0.06	0.05	0.04	0.06	0.03	0.04
W	*0.04*	1.61	1.03	1.82	2.14	3.54	1.72	2.04	1.07	1.09
Re	*0.01*	0.86	0.42	0.60	0.96	0.99	0.67	0.73	0.71	0.29
Os	*0.05*	8.27	4.33	9.38	12.02	15.43	8.40	6.88	6.76	3.62
Ir	*0.01*	6.31	3.76	6.97	7.71	9.58	6.24	6.12	5.38	3.55
Pt	*0.05*	8.61	6.06	9.44	10.42	11.41	8.62	7.98	7.64	6.10
Au	*0.02*	0.65	0.60	0.63	0.60	0.69	0.63	0.63	0.57	0.62
	52	62	63	64	65	66	67	68	69	70
P	2017	1679	1649	1696	1779	1862	1909	1980	2186	1915
S	594	667	631	1267	710	608	964	488	542	529
Ti	16.2	21.1	26.1	23.3	19.6	16.8	16.9	14.3	15.1	16.8
V	0.52	0.18	0.18	0.28	0.18	0.45	0.71	0.64	0.55	0.57
Cr	68.3	81.5	115.1	408.1	104.0	74.0	412.7	69.6	67.0	64.8
Fe	930,000	933,000	933,000	933,000	934,000	933,000	934,000	933,000	935,000	934,000
Co	3280	3170	3220	3250	3230	3220	3180	3200	3250	3200
Ni	66,600	63,600	63,500	62,900	63,000	63,800	62,300	64,100	61,600	63,200
Cu	44.8	42.8	42.8	42.9	41.7	42.1	40.5	42.3	39.2	39.5
Zn	0.26	0.14	0.26	0.24	0.16	0.26	0.27	0.26	0.34	0.41
Ga	1.91	1.79	1.83	1.96	1.75	1.85	1.71	1.77	1.87	1.81
As	3.53	3.44	3.43	3.49	3.26	3.66	3.62	3.62	4.35	3.79
Mo	10.4	8.95	7.22	10.8	10.3	11.7	14.1	12.7	13.4	14.3
Ru	7.03	6.13	5.79	7.22	6.97	7.55	8.81	7.60	8.07	8.82
Rh	1.86	1.84	1.66	1.90	2.14	1.98	2.25	2.17	2.21	2.39
Pd	4.46	4.15	3.91	4.67	4.57	4.41	4.35	4.55	4.42	4.73
Sb	0.03	0.06	0.04	0.09	0.06	0.06	0.06	0.04	0.05	0.04
W	1.45	1.31	1.11	1.82	1.75	1.99	3.39	2.15	3.04	3.54
Re	0.72	0.60	0.24	0.60	0.87	1.02	1.13	0.99	1.25	1.49
Os	8.43	7.09	4.82	9.38	8.48	10.1	15.5	11.0	13.4	16.8
Ir	6.71	5.02	4.05	6.97	6.21	6.85	10.2	7.57	9.32	10.7
Pt	9.35	7.61	7.32	9.44	8.85	10.0	11.5	9.40	11.0	12.1
Au	0.64	0.58	0.62	0.63	0.59	0.76	0.59	0.63	0.53	0.55
	71	72	26	32	46	35	38	27	31	39
P	1947	2058	1397	1380	1487	1270	1325	1220	1327	1367
S	413	476	462	249	573	229	888	453	327	280
Ti	18.5	12.9	39.1	63.8	22.3	48.8	30.7	31.1	37.2	43.5
V	0.28	0.20	0.40	0.37	0.14	0.23	0.23	0.42	0.28	0.19
Cr	78.9	92.1	108	62.6	95.0	121	229	128	78.2	89.5
Fe	933,000	934,000	929,000	928,000	932,000	929,000	932,000	931,000	930,000	929,000
Co	3190	3200	3280	3270	3240	3280	3250	3250	3260	3260
Ni	63,900	63,100	67,700	68,300	64,400	66,700	64,100	65,900	66,300	68,000
Cu	42.1	41.9	48.4	46.7	46.2	48.9	44.2	47.9	45.8	51.1
Zn	0.25	0.31	0.25	0.47	0.14	0.46	0.28	0.31	0.07	0.45

TABLE 1. *Continued*. Major and trace element abundances in metal of the Sierra Gorda 013 lithology 1 (ppm).

	71	72	26	32	46	35	38	27	31	39
Ga	1.80	1.85	2.32	2.32	1.96	2.35	2.29	2.09	2.08	2.16
As	3.61	3.83	3.91	3.77	3.03	3.36	3.36	3.94	4.19	3.21
Mo	8.4	13.5	4.33	4.73	5.95	5.40	8.00	3.25	3.89	4.25
Ru	6.34	8.54	2.00	1.67	3.62	2.06	5.07	2.22	2.30	1.86
Rh	1.83	2.27	0.61	0.47	1.31	0.46	1.54	0.71	0.76	0.55
Pd	4.48	5.02	2.99	3.30	3.74	2.92	3.76	3.45	3.23	3.23
Sb	0.04	0.04	0.14	0.05	0.06	0.23	0.10	0.05	0.08	0.12
W	1.61	3.88	0.16	0.12	0.35	0.40	0.35	0.20	0.22	0.12
Re	0.55	1.96	b.d.l	b.d.l	0.05	0.03	0.28	0.13	0.10	0.07
Os	6.24	14.7	0.22	0.13	1.57	0.10	2.66	0.47	0.40	0.27
Ir	5.16	10.2	0.28	0.20	1.70	0.15	2.82	0.56	0.52	0.39
Pt	7.52	11.4	1.28	0.84	4.15	1.11	6.04	1.99	1.54	1.39
Au	0.46	0.56	0.64	0.61	0.51	0.66	0.48	0.63	0.63	0.47
	40	47	33	55	37	45	54	25	28	29
P	1248	1363	1203	1373	1248	1475	1217	1432	1510	1503
S	441	539	123	725	280	238	416	448	290	271
Ti	41.9	29.2	84.1	31.1	38.5	33.0	32.0	448	47.5	53.1
V	0.06	0.18	0.16	0.29	0.24	0.13	0.09	0.43	0.60	0.60
Cr	112	121	119	69	136	88.7	108	81.5	62.6	68.2
Fe	931,000	931,000	931,000	932,000	931,000	935,000	931,000	930,000	932,000	929,000
Co	3270	3210	3190	3210	3190	3320	3180	3320	3260	3270
Ni	65,600	65,300	66,000	65,200	65,500	62,000	65,400	66,600	65,100	67,600
Cu	46.8	46.3	47.3	48.1	47.2	44.0	50.2	48.4	45.6	47.5
Zn	0.37	0.34	0.39	0.20	0.30	0.31	0.11	0.27	0.34	0.39
Ga	2.28	2.09	2.40	2.19	2.09	2.13	2.25	2.19	2.45	2.25
As	2.65	2.62	4.66	3.78	3.18	3.15	3.78	4.45	4.82	5.22
Mo	4.31	6.09	4.80	4.59	4.25	3.96	3.55	4.46	4.63	4.76
Ru	2.57	3.72	1.16	2.75	2.28	2.18	1.98	2.15	1.88	2.14
Rh	0.78	1.04	0.39	0.90	0.54	0.62	0.54	0.53	0.70	0.56
Pd	3.32	3.63	2.32	3.19	3.25	2.76	2.48	3.39	3.33	2.56
Sb	0.11	0.08	0.08	0.10	0.15	0.08	0.14	0.10	0.08	0.09
W	0.08	0.13	0.06	0.30	0.12	0.04	0.04	0.17	0.16	0.17
Re	0.07	0.11	0.07	0.10	0.11	0.08	0.04	0.02	0.01	0.02
Os	0.62	1.62	0.08	0.80	0.62	0.07	0.13	0.22	0.14	0.39
Ir	0.71	1.55	0.08	1.00	0.46	0.49	0.35	0.44	0.52	0.24
Pt	2.41	3.43	0.64	2.41	1.51	1.21	1.21	1.66	1.34	1.04
Au	0.53	0.48	0.53	0.68	0.56	0.50	0.49	0.57	0.57	0.63

	30	34	36	41	43	42	44	53
P	1318	1371	1325	1130	1210	1249	1421	1296
S	236	222	175	222	2414	172	408	547
Ti	60.2	45.2	93.2	58.7	72.6	47.1	36.5	30.5
V	0.33	0.34	0.08	0.18	8.31	0.14	0.15	0.15
Cr	116	110	88.7	158	1967	142	131	109
Fe	931,000	931,000	929,000	930,000	927,000	931,000	932,000	931,000
Co	3210	3250	3230	3230	3260	3200	3240	3220
Ni	65,900	65,900	67,600	66,600	68,000	65,700	65,000	66,000
Cu	47.2	48.5	53.7	49.0	53.7	48.1	46.7	49.5
Zn	0.27	0.47	1.02	0.60	1.34	0.64	0.20	0.13
Ga	2.39	2.23	3.11	2.43	2.72	2.11	2.18	2.01
As	4.63	3.32	4.35	3.19	3.27	3.15	3.26	3.65
Mo	4.15	3.90	4.70	4.49	5.42	4.44	3.81	5.00
Ru	1.97	2.09	1.73	1.86	1.44	1.60	2.08	2.91
Rh	0.65	0.56	0.31	0.43	0.28	0.53	0.66	0.84
Pd	3.16	2.91	2.62	2.79	2.26	2.72	3.35	3.37
Sb	0.04	0.29	0.38	0.14	0.13	0.15	0.11	0.10
W	0.14	0.09	b.d.l	0.12	0.24	b.d.l	0.21	0.12
Re	b.d.l	b.d.l	b.d.l	0.03	0.06	0.09	b.d.l	0.06

TABLE 1. *Continued*. Major and trace element abundances in metal of the Sierra Gorda 013 lithology 1 (ppm).

	30	34	36	41	43	42	44	53
Os	0.06	0.27	b.d.l	0.19	0.20	0.03	0.61	1.25
Ir	0.34	0.53	0.01	0.44	0.08	0.24	0.55	0.90
Pt	1.33	1.33	0.49	0.76	0.93	1.01	1.53	2.78
Au	0.50	0.58	0.39	0.59	0.63	0.42	0.49	0.72

Abbreviation: b.d.l., below detection limit.

and L2. This is a consequence of the fact that the large metal globules were built up from smaller metal grains (Lorenz et al., 2023).

Plots of Ir and Re versus Ni (Figure 7a,b) show that metal globules from L1 form trends parallel to those of many magmatic iron groups (e.g., IC, IIA, IIB, IIIAB, and IVA). These trends cross the CBa metal field, CH/CBb zoned metal field, and the CI metal trend lines (Figure 7a, b). In contrast, the metal from L2 concentrates around the middle of the L1 metal trend and below the CI correlation but is offset with higher Ni contents (Figure 7a,b).

In Figure 8, we plot Os versus Ir data for metals from L1 and L2. The SG 013 L1 data show a positive correlation between Os and Ir, with a slope inclined with respect to the CI correlation. Several points with very low Os and Ir lie off this trend. The trend is similar to that of some magmatic irons (e.g., IIAB, IIIAB, IVB, and IIIF) (Figure 8). Unlike L1, the metal from L2 concentrates at the lower half of the L1 correlation and on the CI correlation line (Figure 8).

Tungsten versus Fe concentrations of the L1 metal, normalized to Ni and CI chondrites, demonstrate a trend which is almost parallel to that of IIAB irons (Figure 9). The L1 metal with the highest W content has a slightly different slope compared to the one with the lower W content. Similar to Figure 7, the L2 metal has a more limited range of W/Ni than the L1 metal trend, concentrating around the CI chondrite ratio (Figure 9).

Palladium versus Ni concentrations in the L1 metal show a linear trend with a weak negative correlation compared to the CB and CR metal, which form fields of composition. The L1 trend crosses the trends of CI metal composition and the CH/CBb-zoned metal grains (Figure 10). The Pd concentrations in the L2 metal are in the L1 range of compositions (Figure 10). Unlike the L1 metal, Pd from the metal of L2 forms a cluster near the CB chondrites field. The distribution of W versus Ir in the L2 metal is different from that of the L1 metal composition and forms a cluster located above the L1 metal trend (Figure 11). Concentrations of Mo and Pd co-vary with Ir for the L1 metal, and the L2 metal compositions are located on the L1 trends (Figure 11).

Gold, As, and Ga in both lithologies have no correlations with Ni. Gold and Ga contents in the L1 and L2 metal fall within the CB chondrites metal field (Figure 12a,b). The L2 metal is depleted in Au and enriched in Ni compared to the L1 metal (Figure 12a). Gallium concentrations from both lithologies show a tighter range (Figure 12b). However, while correlation is not obvious for individual groups, when L1 and L2 are taken together, they define a correlation in Au-Ni space (Figure 12a) and the characteristic 'bean' shape in the Ga-Ni space (Figure 12b).

DISCUSSION

Formation of the L1 Metal

Based on a previous study (Ivanova et al., 2022; Krot et al., 2023; Lorenz et al., 2023), the SG 013 CB-like chondrite was formed by re-accretion after the plume processes produced by a catastrophic impact event, like other CB chondrites (Campbell et al., 2002; Fedkin et al., 2015; Kallemeyn et al., 1978; Koefoed et al., 2022; Krot et al., 2005, 2022; Oulton et al., 2016; Petaev et al., 2001; Wasson & Kallemeyn, 1990; Weyrauch et al., 2019). The SG 013 lithology 1 does not contain the fine-grained matrix between chondrules like all other CB chondrites. The lack of the fine-grained matrix may have been due to the origin of CB chondrites in the impact plume (Stewart et al., 2019a, 2019b).

The major and trace element compositions of the metal globules of L1 and metal particles of L2 obtained by LA-ICP-MS at the 100–150 μm scale effectively integrating over the exsolved Fe-Ni phases observed by the EMPA at the 1-micron scale and are the best average content of several analyses. First, we discuss geochemistry and formation of the L1 metal. Although Co and Ni contents of the L1 metal globules are in the CB chondrites field (Figure 4), the Ni and Co distribution of the L1 metal is different from the CH/CBb zoned metal composition trend and is similar to that of magmatic groups of irons possibly indicating a magmatic origin of the L1 metal (Figure 4b). Wasson and Richardson (2001) and Wasson and Choi (2003) discussed the magmatic trends in IIIAB, IVA irons and pallasites and emphasized that Ni-Au, Co-Au and, therefore, Co-Ni-positive trends correspond to magmatic trends. It was also shown experimentally by Chabot et al. (2003) that D_{Ni} and D_{Co} is sharply increased up to >1 with increasing of the S content in a melt.

TABLE 2. Major and trace element abundances in metal (in ppm) of the Sierra Gorda 013 lithology 2 (ppm).

	D. L.	1	2	3	4	5	6	7	8	9	10	11	12	13
P		n.a.	n.a.	n.a.	n.a.	n.a.	n.a.	n.a.	n.a.	n.a.	n.a.	n.a.	n.a.	n.a.
S		n.a.	n.a.	n.a.	n.a.	n.a.	n.a.	n.a.	n.a.	n.a.	n.a.	n.a.	n.a.	n.a.
Ti		n.a.	n.a.	n.a.	n.a.	n.a.	n.a.	n.a.	n.a.	n.a.	n.a.	n.a.	n.a.	n.a.
V	*0.01*	1.04	0.76	3.76	0.94	0.59	0.78	0.62	0.69	0.50	0.52	0.72	0.65	0.47
Cr	*0.0*	57.3	44.1	108	48.7	47.0	44.4	47.5	46.6	43.2	42.3	46.4	48.2	48.5
Fe	*1*	903,000	924,000	921,000	922,000	924,000	914,000	923,000	926,000	925,000	925,000	918,000	924,000	925,000
Co	*0.02*	3250	3200	3020	3140	3070	3000	2970	3060	3000	3110	3190	3070	3150
Ni	*0.06*	71,800	69,800	72,500	71,800	69,900	69,500	71,500	69,400	70,200	70,500	77,100	71,600	70,500
Cu	*0.2*	44.6	38.4	41.4	44.2	37.9	36.3	39.6	38.0	38.4	36.9	41.0	40.0	38.7
Zn	*0.02*	1.17	0.44	0.42	0.42	0.34	0.31	0.34	0.30	0.29	0.57	0.65	0.57	0.47
Ga	*0.01*	2.14	2.15	2.30	2.21	1.98	1.88	2.36	2.26	2.15	2.10	2.03	1.84	2.05
As	*0.00*	5.18	3.75	3.27	3.15	3.29	2.59	2.58	3.02	2.58	2.34	3.05	2.45	2.51
Mo	*0.01*	2.55	4.50	4.34	3.67	4.52	4.11	5.30	4.59	1.99	3.89	5.41	4.38	3.99
Ru	*0.0002*	2.10	2.47	2.94	2.67	2.39	2.76	2.94	2.83	2.53	2.46	2.19	1.92	1.84
Rh	*0.0001*	0.48	0.55	0.63	0.68	0.52	0.58	0.51	0.59	0.44	0.36	0.43	0.30	0.34
Pd	*0.00003*	2.96	2.84	3.14	3.39	2.79	2.69	2.95	3.68	2.87	3.28	3.09	3.06	2.90
Sb	*0.001*	0.12	0.18	0.19	0.28	0.13	0.11	0.15	0.14	0.14	0.19	0.23	0.16	0.18
W	*0.003*	0.96	0.65	0.37	0.42	0.55	0.81	0.69	0.30	0.65	0.40	0.41	0.50	0.68
Re	*0.0003*	0.07	0.12	0.06	0.10	0.08	0.11	0.11	0.05	0.09	0.12	0.04	0.08	0.11
Os	*0.002*	0.51	0.57	0.72	0.56	0.92	0.94	1.07	0.68	1.19	0.85	0.37	0.68	0.52
Ir	*0.002*	0.59	0.67	0.69	0.75	0.86	0.95	0.97	0.82	0.80	0.96	0.60	0.38	0.48
Pt	*0.005*	1.41	1.81	2.44	2.06	2.45	2.66	2.68	2.92	2.56	2.36	1.91	1.41	2.09
Au	*0.002*	0.30	0.21	0.33	0.37	0.39	0.28	0.30	0.31	0.31	0.33	0.30	0.32	0.31

	14	15	16	17	18	19	20	21	22	23	24	25	Average	σ
P	n.a.	n.a.	n.a.	n.a.	n.a.	n.a.	n.a.	n.a.	n.a.	n.a.	n.a.	n.a.		
S	n.a.	n.a.	n.a.	n.a.	n.a.	n.a.	n.a.	n.a.	n.a.	n.a.	n.a.	n.a.		
Ti	n.a.	n.a.	n.a.	n.a.	n.a.	n.a.	n.a.	n.a.	n.a.	n.a.	n.a.	n.a.		
V	0.72	0.62	1.06	0.50	0.54	0.38	0.30	1.49	0.30	0.28	0.77	0.99	0.80	0.68
Cr	48.5	49.2	47.2	41.9	46.1	44.8	42.9	186.7	39.9	41.3	53.5	44.8	54.3	30.4
Fe	925,000	925,000	927,000	919,000	926,000	926,000	924,000	927,000	922,000	925,000	926,000	925,000	923,000	5120
Co	3130	3110	3500	2920	3340	3270	3160	3100	3070	3290	3500	3300	3160	150
Ni	70,900	70,100	67,900	76,500	69,500	68,700	71,500	68,600	73,700	70,300	69,000	70,200	71,000	2200
Cu	41.5	39.5	45.5	45.3	41.9	40.6	41.9	38.6	42.2	39.4	47.8	43.1	40.9	2.92
Zn	0.39	0.40	0.55	0.40	0.58	0.64	0.58	0.56	0.56	0.73	0.81	0.46	0.52	0.19
Ga	2.35	2.41	2.29	2.27	2.07	2.10	2.01	2.10	1.96	2.14	2.20	2.31	2.15	0.15
As	2.82	2.54	4.26	3.59	2.56	3.56	3.15	2.94	2.86	2.61	4.84	3.54	3.16	0.73
Mo	3.01	2.09	3.33	3.09	2.29	3.52	3.61	2.73	2.14	2.62	3.70	4.51	3.59	0.99
Ru	2.06	2.14	2.36	2.42	2.12	1.91	2.02	2.17	2.06	1.95	2.78	2.93	2.36	0.36
Rh	0.51	0.41	0.54	0.70	0.46	0.37	0.41	0.44	0.51	0.45	0.60	0.59	0.50	0.10
Pd	2.92	2.68	3.61	4.09	2.77	2.99	3.49	2.92	3.57	2.87	3.52	3.85	3.16	0.39
Sb	0.17	0.10	0.37	0.18	0.06	0.11	0.10	0.11	0.24	0.15	0.40	0.19	0.17	0.08
W	0.51	0.34	0.50	0.41	0.52	0.24	0.78	0.44	0.39	0.44	0.30	0.41	0.51	0.18
Re	0.13	0.10	0.10	0.11	0.06	0.07	0.06	0.11	0.09	0.07	0.05	0.07	0.09	0.03
Os	1.26	1.05	0.71	1.07	0.38	0.33	0.81	0.56	0.57	0.47	0.37	0.44	0.70	0.28
Ir	0.65	0.72	0.78	1.19	0.45	0.53	0.63	0.44	0.67	0.51	0.59	0.92	0.70	0.20
Pt	1.88	2.31	1.35	2.67	1.48	1.52	2.19	1.84	2.25	1.77	1.79	2.56	2.09	0.46
Au	0.25	0.33	0.30	0.31	0.40	0.32	0.30	0.33	0.28	0.29	0.29	0.30	0.31	0.04

Abbreviation: n.a., not analyzed.

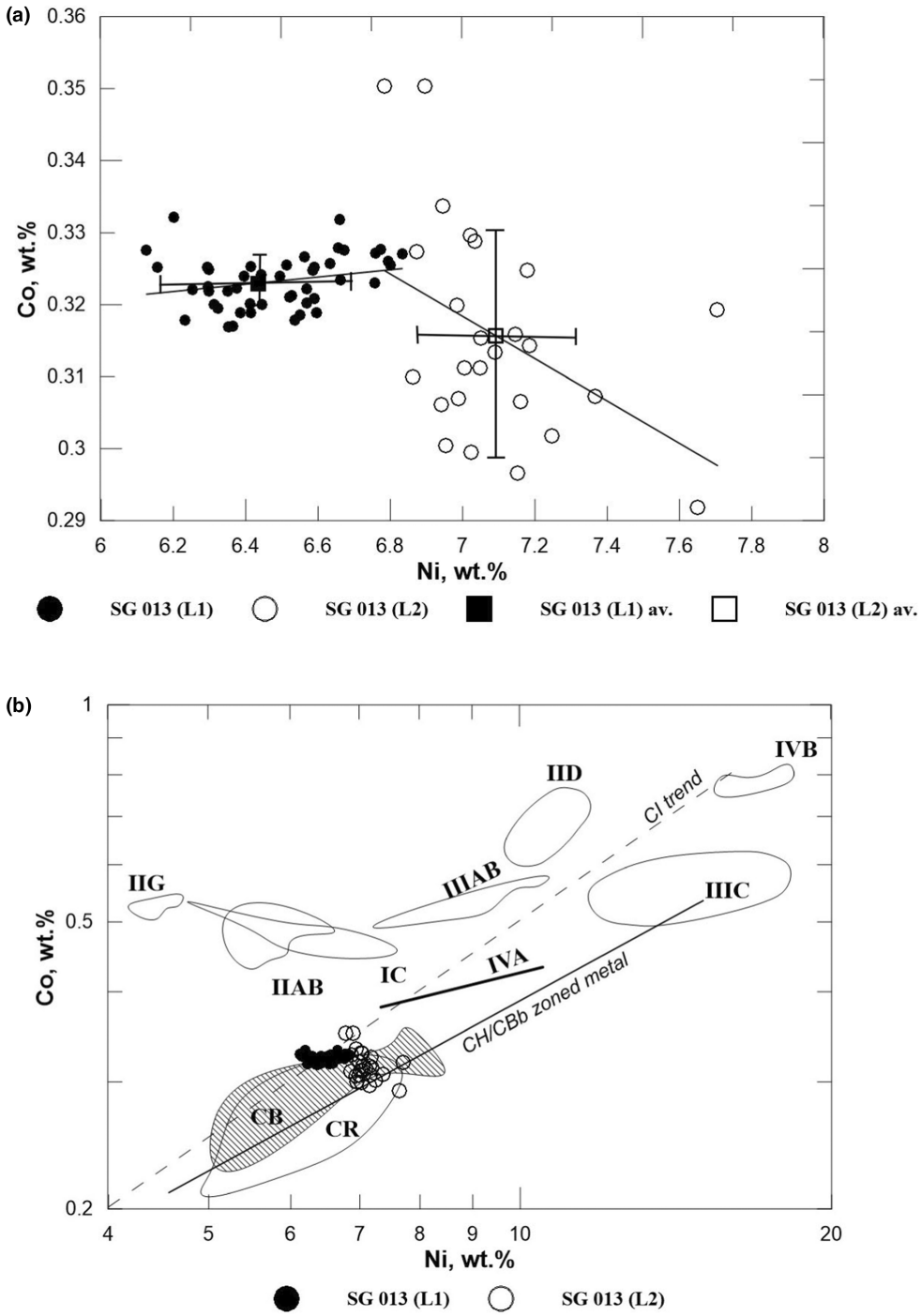

FIGURE 4. (a) The Ni and Co abundances of SG 013 metal acquired by LA-ICP-MS; squires and bars—average volumes and standard deviations; lines—linear trends. (b) Co-Ni distribution in the SG 013 metal of lithologies 1 (L1) and 2 (L2) compared to the metal composition from CR (Kong et al., 1999; Kong & Palme, 1999; van Kooten et al., 2022), unzoned metal from CH, CB chondrites (shown as CB) and trend of zoned metal from CH/CBb chondrites (Campbell et al., 2001, 2002; Weyrauch et al., 2019), CI (Anders & Grevesse, 1989), and magmatic iron meteorites IC (Tornabene et al., 2023), IIAB (Wasson et al., 2007), IIIAB (Wasson, 1999), IID, IIIC (Scott, 1972; Scott & Wasson, 1975), IIE (Wasson, 2017), IIF (Hilton et al., 2020), IVA (Wasson & Richardson, 2001), and IVB (Campbell & Humayun, 2005).

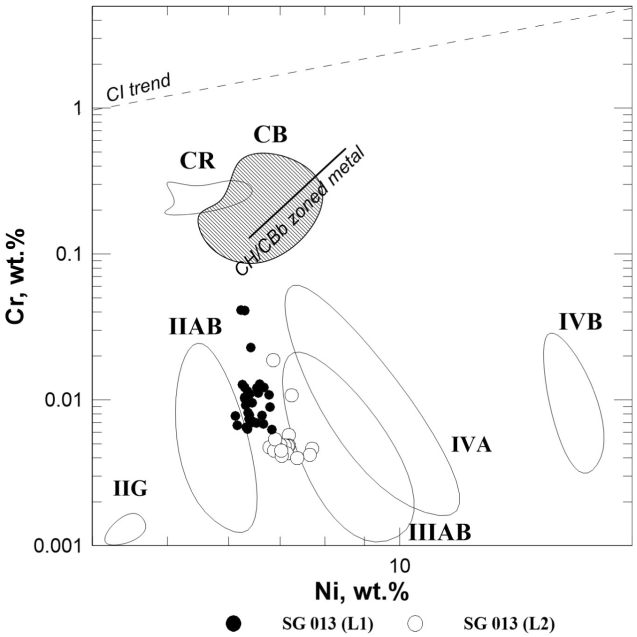

FIGURE 5. Cr-Ni distribution in the SG 013 metal of lithologies 1 (L1) and 2 (L2) compared to the metal composition from CR (Kong et al., 1999; Kong & Palme, 1999), unzoned metal from CH, CB chondrites (shown as CB) and trend of zoned metal from CH/CBb chondrites (Campbell et al., 2001, 2002; Weyrauch et al., 2019), CI composition (Anders & Grevesse, 1989), and magmatic iron meteorites IC (Tornabene et al., 2023), IIAB (Wasson et al., 2007) IIIAB (Wasson, 1999), IIG (Wasson & Choe, 2009), IVA (Wasson & Richardson, 2001), and IVB (Campbell & Humayun, 2005).

Therefore, the positive Ni-Co trend in magmatic irons and a slightly positive trend in the SG 013 L1 (Figure 4a) could be explained by gradually increasing of S in a liquid fraction during fractional crystallization and, respectively, enrichment in Ni and Co of a solid fraction.

The systematic depletion of L1 metal in Cr relative to CB chondrites and similar to several groups of magmatic irons (Figure 5) probably was a pre-impact peculiarity of the metal and indicates its magmatic origin in the parent body core. Magmatic iron meteorites have negative correlations of Cr with Ni, which may reflect crystallization of chromite (Chabot & Drake, 2000; Jones & Drake, 1983) or distribution of chromium in S-rich immiscible liquid (e.g., Haack & Scott, 1992). In the magmatic precursor of the SG 013 metal, the same processes could take place. Chromite is widespread in the SG 013 rock, mostly along the boundaries between metal and chondrules (Hoffman, 2021; Ivanova et al., 2022). Chromite as well as daubréelite also occurs inside the metal globules of L1 (Lorenz et al., 2023). Either chromite is a product of crystallization in a core of the precursor body, or it is a product of oxidation of Cr and Fe in the plume and was trapped in the metal globules.

The chemical variations within magmatic iron groups for nearly all trace elements are consistent with the trends expected during fractional crystallization of a large volume of molten Fe-Ni-S metal such as an asteroidal core (e.g., Chabot & Haack, 2006; Wasson, 1999). The SG 013 L1 metal shows correlations of HRSE like those of magmatic irons (Figure 7a,b). Alternatively, if a condensation process was responsible for SG 013 metal formation, the correlations in Ir-Ni and Re-Ni space similar to CI chondrites and CH/CBb metal should be observed for SG 013 metal (Campbell et al., 2001; Weyrauch et al., 2019), which is not the case (Figure 7a,b).

The positive linear trend of Os versus Ir in the metal from SG 013 L1 is similar to those of magmatic iron meteorites (Figure 8). The very large variations of Ir within groups of magmatic irons (Figure 7a) are due to their formation during fractional crystallization of the Fe-Ni-S melt and Ir partition coefficient solid/liquid $D > 1$ resulted in preferential distribution of Ir into a solid phase (Chabot et al., 2003). Similar to Ir, Os also has distribution coefficient >1 and is compatible with a solid phase in contrast to elements with $D < 1$ which are incompatible with a solid phase and preferential distributing into a liquid. The positive linear trend of Os versus Ir in magmatic iron meteorites inclined relative to the CI chondrite trend (Figure 8) should originate from early accumulation of solid metal phase from the S-enriched Fe-Ni melt where D_{Os} became > D_{Ir} compared to the pure Fe-Ni melts (Chabot et al., 2003). If the L1 Os-Ir trend originates from the fractional crystallization of the metal liquid similar to irons, the L1 metal includes the full range of fractional crystallization products from the metallic core (Figure 8). Note that the correlation of Os and Ir is weaker at low concentrations of Os and Ir in depleted portions of the metal due to statistical uncertainty of the analyses.

The abovementioned chemical similarity of SG 013 L1 metal with magmatic irons points to a magmatic origin in the core of a planetesimal. To test this hypothesis, we modeled the fractional crystallization (FC) of CR-like chondrite metal (Figure 6b) taking into consideration that based on chemical and isotopic similarities CH and CB chondrites belong to the CR chondrite clan (Weisberg et al., 1995) and formed in an isotopically similar disk reservoir (van Kooten et al., 2016).

Our calculations were presented in detail in the publication of Teplyakova et al. (2022) to explain the formation of IIE irons, and we used this approach for the FC model to explain the SG 013 metal formation. In this model, distribution coefficients for siderophile elements were calculated as functions of the molar fraction of sulfur (Xs) in accordance with the model and parameters of Chabot and Jones (2003), Chabot et al. (2003), and Chabot et al. (2009). A batch of equilibrium liquids formed by fractional crystallization

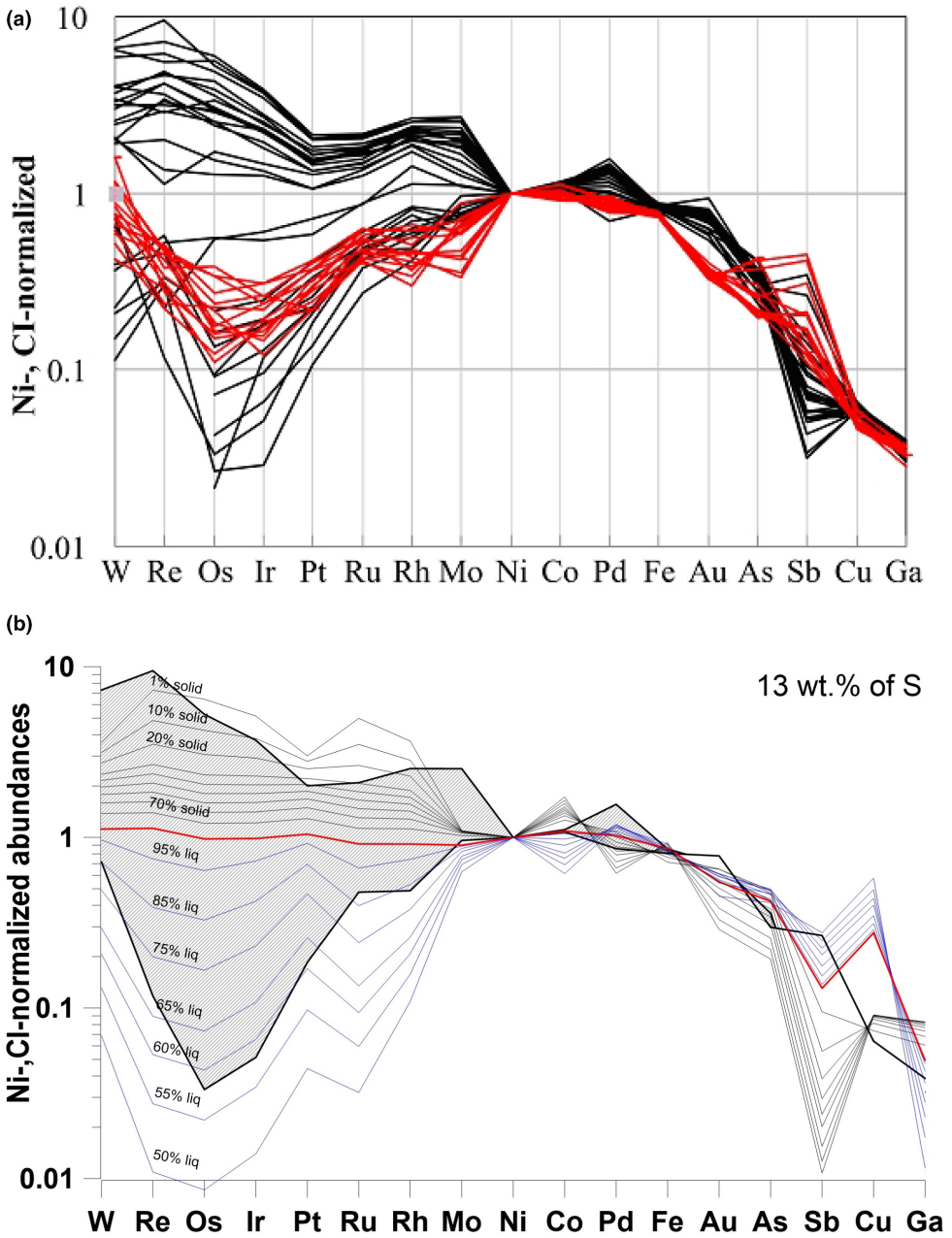

FIGURE 6. (a) Trace elements distribution in the SG 013 metal of lithology 1 (black lines) and Ni-rich metal of lithology 2 (red lines); (b) equilibrium liquids formed by fractional crystallization (FC) of the CR-like metal model liquids (blue lines), calculated at 10% melting intervals using partition coefficients that tracked the sulfur content 13 wt% of S of the liquid using the formalism of Chabot et al. (2009), and corresponding solid metal composition (black lines) compared to similar calculation so FC at different S contents: (c) 5 wt%, (d) 10 wt%, (e) 15 wt%, and (f) 18 wt%. Average CR chondrite metal composition (Kong et al., 1999) is shown as a red line. (Color figure can be viewed at wileyonlinelibrary.com)

of the CR chondrite metal is given as blue lines (Figure 6b), calculated at 10% melting intervals. The last melted liquid fraction was restricted by $F_L \sim 26\%$ since during the progressive crystallization the bulk S abundance in the liquid reaches the S content of the Fe-FeS eutectic. The fractional melts should be enriched in the incompatible elements Pd, Au, As, Sb, Cu, and Ga, and depleted in compatible elements W, Re, Os, Ir, Pt, Ru, and Mo relative to the starting composition, since incompatible elements are accumulated in the residual liquids due to partition coefficients between solid and liquid <1. A complementary effect is observed in the solid metal fractions (Figure 6b) in equilibrium with each of these fractional melts. The calculations showed that the

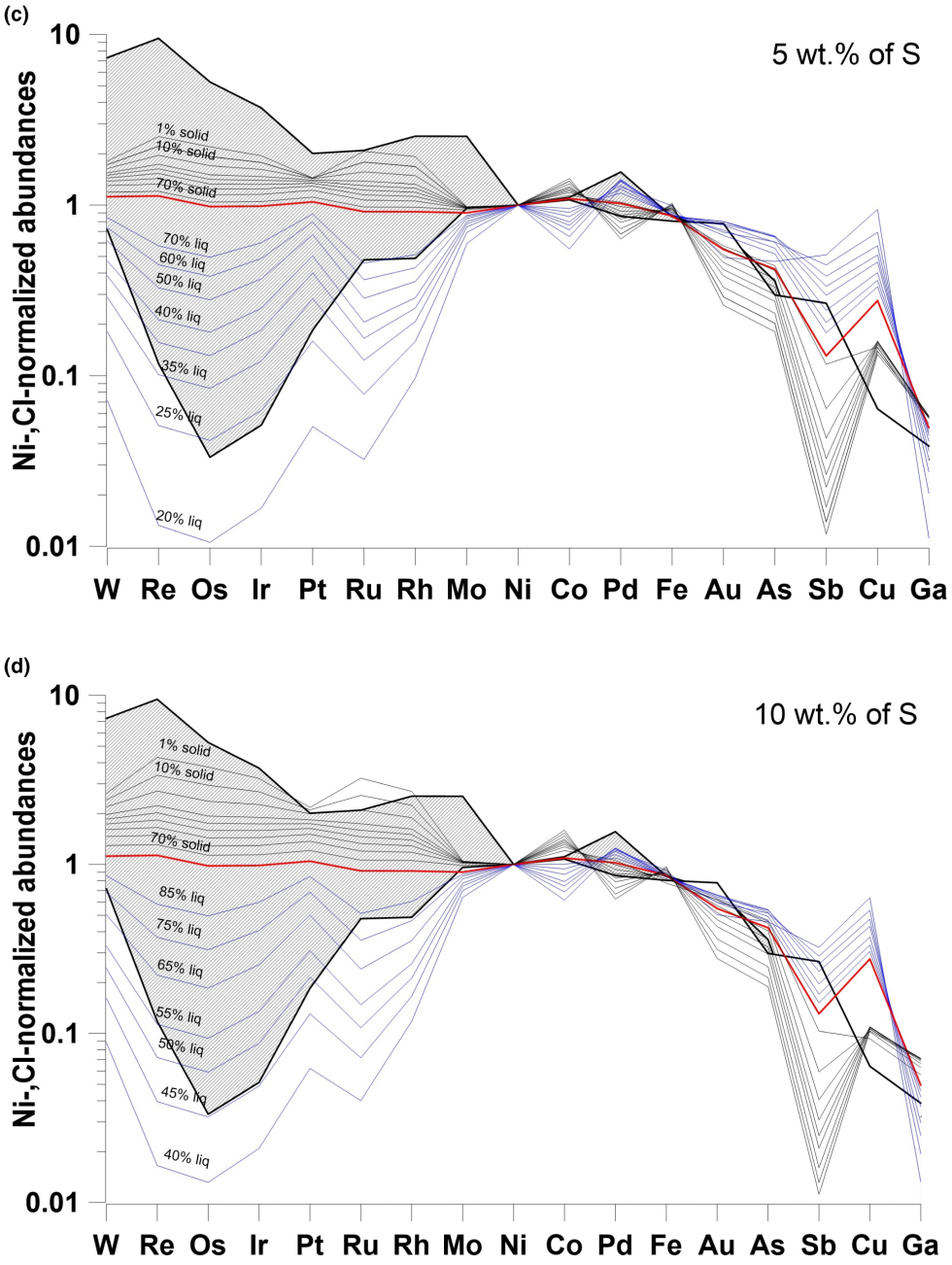

FIGURE 6. *Continued.*

initial model metal composition should contain 13 wt% of S to better fit the siderophile distribution of the SG 013 metal compared to other S contents used in the model calculations – 5, 10, 15, and 18 wt% (Figure 6b–f).

According to the FC model, W and Mo also accumulate in solid metal fractions in the L1 metal and correlate with Ir, which is compatible with a solid metal phase indicating reduced conditions of environment (Figure 11). We predict that Pd should be enriched in the liquid metal phase as an incompatible element and should demonstrate a positive correlation with Ni and a negative correlation with Ir, similar to magmatic irons. However, Pd in L1 metal is negatively correlated with Ni (Figure 10) and positively correlated with Ir (Figure 11). As such, these correlations cannot be explained by the fractional crystallization of a solid phase from metal liquid. Phosphorous and carbon could not affect fractional crystallization significantly. With increasing P-content of the metallic liquid, Pd showed a constant partition coefficient (Corrigan et al., 2009), and with

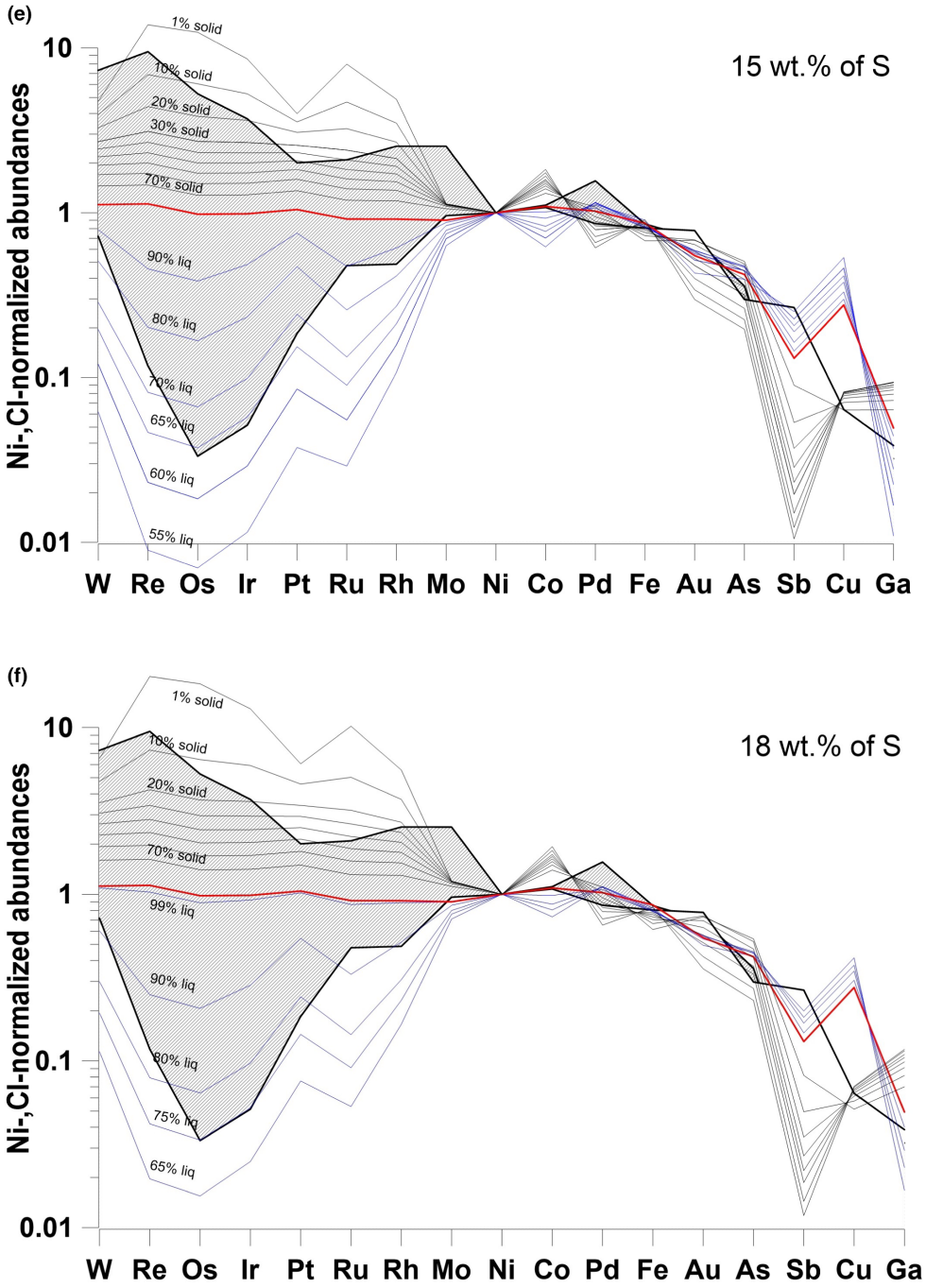

FIGURE 6. *Continued.*

increasing C content of the liquid, the partition coefficients of the majority of the elements, including Pd, were increased (Chabot et al., 2006). The effect was analogous to that of S for many elements, including Pd.

We considered two alternative processes that could provide a positive correlation of Pd and Ir: (1) the capture of residual liquid during the growth of dendritic crystals as it was shown in Haack and Scott (1992) and (2) recondensation of Pd in a plume. Concerning the process (1), mixing of the residual liquid and solid phase in different proportions at each stage of fractional crystallization could produce a set of compositions in which Pd will be positively correlated with Ir. However, other incompatible trace elements should also exhibit pseudo-compatible behavior that was not observed. Concerning the process (2), palladium becomes

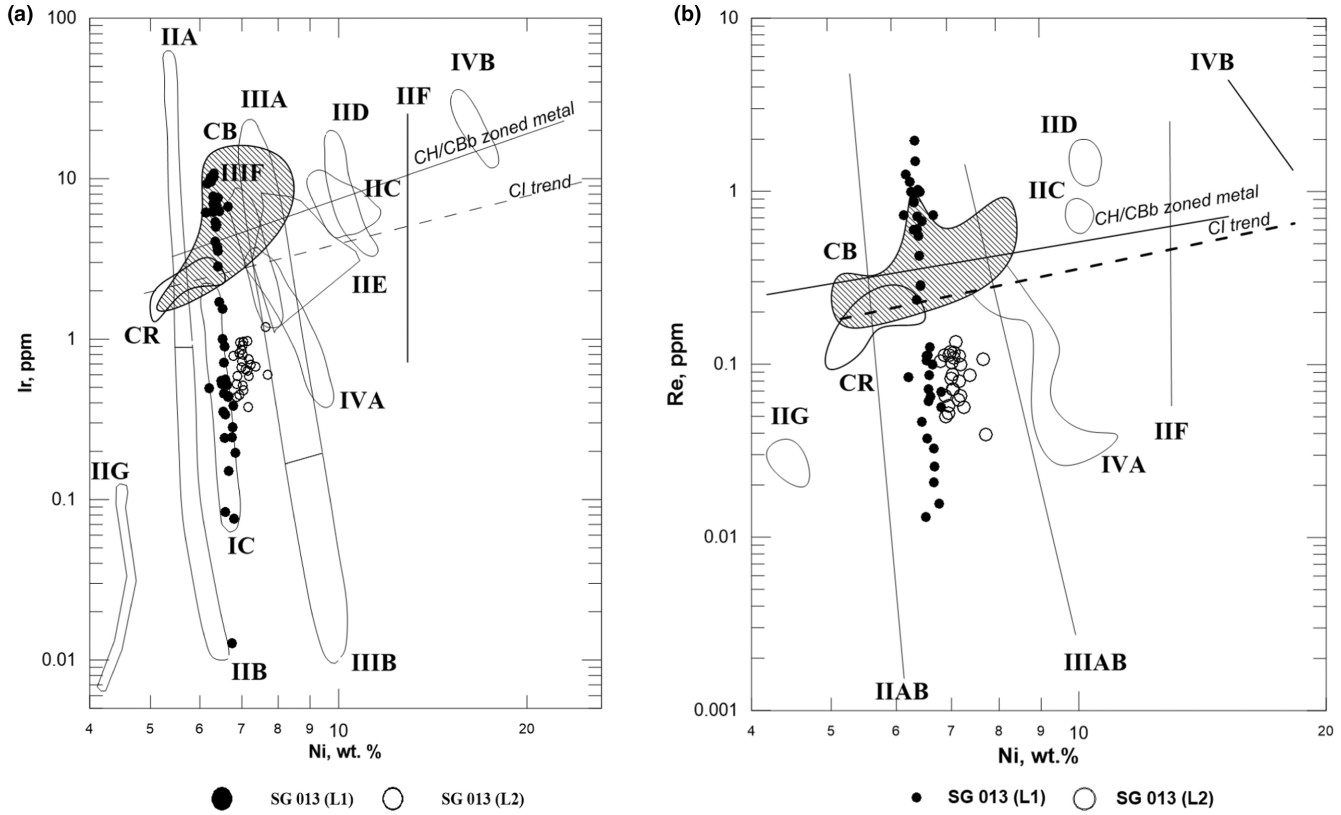

FIGURE 7. Logarithmic plots of Ir against Ni (a) and Re against Ni (b) in the SG 013 metal of lithologies 1 (L1) and 2 (L2) compared to the metal composition from CR (Kong et al., 1999; Kong & Palme, 1999, unzoned metal from CH, CB chondrites (shown as CB), and trend of zoned metal from CH/CBb chondrites (Campbell et al., 2001, 2002; Weyrauch et al., 2019) CI composition (Anders & Grevesse, 1989), and magmatic iron meteorites IC (outlined area from Scott, 1972), IIAB (Wasson et al., 2007), IIIAB (Wasson, 1999), IIC, IID, IIIC (Scott, 1972; Scott & Wasson, 1975), IIE (Wasson, 2017), IIF (Hilton et al., 2020), IVA (Wasson & Richardson, 2001), and IVB (Campbell & Humayun, 2005).

significantly more refractory than Fe at very high partial pressures of siderophiles (Campbell et al., 2002). Campbell et al. (2002) proposed that the unzoned metal grains and chondrules from CBa chondrites condensed from a plume of material vaporized during an impact at very high metal vapor pressure (10^7 relative to canonical solar nebular). For example, zoned metal grains from QUE 94411 CBb have positively covarying Pd/Ir ratios indicating Pd recondensation (Figure 7 from Campbell et al., 2001). Noncanonical pressure regimes for the formation of the CB metal were confirmed by Fedkin et al. (2015). However, variations of Ir/Ni, Pd/Ni, and Pd/Ir ratios in the L1 metal and their linear trends in the SG 013 L1 metal (Figures 7a, 10, and 11) have different patterns which are opposite to the patterns of Pd/Ni and Ir/Ni distributions during recondensation (Campbell et al., 2001), and Pd/Ni distribution during fractional crystallization (Scott, 1972). Based on these observations, we cannot provide a reliable explanation of the Pd behavior.

The volatile elements Au, As, and Sb in L1 metal, unlike the prediction of fractional crystallization modeling (Figure 6b) show ranges of values, while Cu and Ga have narrow variations (Figure 12a,b). Moreover, due to evaporation in the plume, HRSE-poor L1 metal compositions have lower concentrations of mid-VSE and VSE than those predicted by our fractional crystallization model. Other CB metal compositions demonstrate similar behavior of volatile siderophiles. Considering the likely heterogeneous physical–chemical conditions in the impact plume (Florin et al., 2021; Ivanova et al., 2022; Krot et al., 2023; Lorenz et al., 2023; Weyrauch et al., 2019, 2021), we propose that a different degree of volatilization of some moderately volatile and volatile siderophile elements of the SG 013 metal and probably their recondensation in different regions of the plume overprinted the primary chemical characteristics of their initial magmatic signatures.

Formation of the L2 Metal

In contrast to the L1 metal, the L2 metal is depleted in HRSE compared to the unzoned CH and CBa metal,

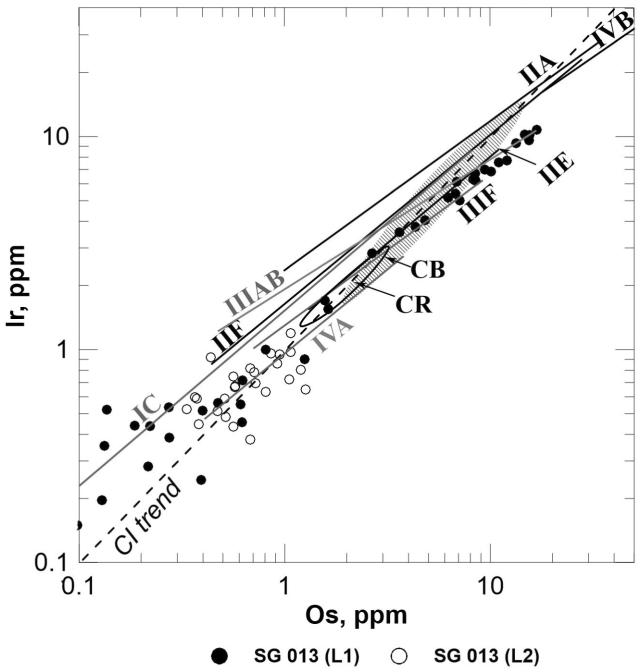

FIGURE 8. Os versus Ir for the metal composition of the SG 013 lithologies 1 (L1) and 2 (L2) compared to the metal composition from CR (Kong et al., 1999; Kong & Palme, 1999), CH-CB chondrites (Campbell et al., 2001, 2002; Weyrauch et al., 2019), CI composition (Anders & Grevesse, 1989), and magmatic iron meteorites IC (Tornabene et al., 2023), IIE (Teplyakova et al., 2022), IIF (Hilton et al., 2020), IIA, IIIAB, IIIF, IVA (Ryan et al., 1990), and IVB (Campbell & Humayun, 2005).

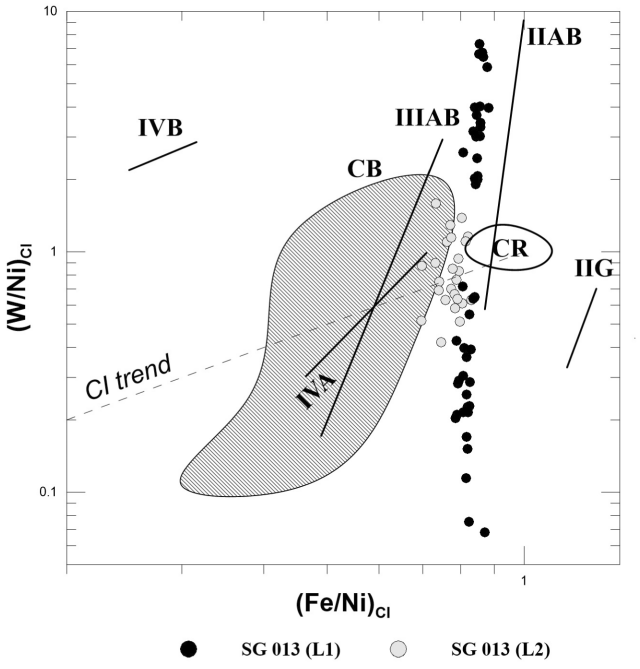

FIGURE 9. Logarithmic plot of $(W/Ni)_{CI}$ against $(Fe/Ni)_{CI}$ for the SG 013 metal of lithologies 1 (L1) and 2 (L2) compared to the metal composition from CR (Kong et al., 1999; Kong & Palme, 1999), CH-CB chondrites (Campbell et al., 2001, 2002; Weyrauch et al., 2019), CI composition (Anders & Grevesse, 1989), and magmatic iron meteorites. Positive correlations are visible in groups IIAB (Wasson et al., 2007), IIE (Wasson, 2017), IIG (Wasson & Choe, 2009), IIIAB Wasson, 1999) IVA (Wasson & Richardson, 2001), and IVB (Campbell & Humayun, 2005) while SG 013 shows a linear vertical trend.

to the zoned CH and CBb metal (Figures 7, 8, and 10) and compared to the early HRSE-rich fractions of fractional crystallization corresponding to several chemical compositions of the L1 metal and discussed in the previous section. The distribution of siderophile elements in the L2 metal does not show any correlations between highly refractory (W, Os, Ir, Re, and Mo) and moderate volatile siderophile elements (Ni, Co, Pd, and Cr) based on Figures 4–11. In formation of the L2 metal, three processes could be discussed: (1) magmatic; (2) plume processing, and (3) thermal metamorphism.

Magmatic Process

In the L2 metal particles, Co does not correlate with Ni (Figure 4a,b), does not follow the magmatic trend and distribution corresponding to the CH/CBb-zoned metal condensate grains. Depletion in Cr in the L2 metal as well as in L1 is similar to that of iron meteorites of the IIAB and IVA chemical groups (Wasson, 1999; Wasson & Richardson, 2001) (Figure 5) and probably connected with the magmatic process of the L2 metal as it was shown in the L1 metal. The linear Os-Ir distribution (Figure 8) and the general depletion of the L2 metal in HRSE compared to HRSE-enriched compositions of the L1 metal population indicate that the L2 metal may represent some late products of the fractional crystallization sequence of the L1 metal which further was affected by the plume processing. However, the L2 metal is enriched in Ni compared to the L1 metal indicating that other process(es) affected the L2 metal composition.

Plume Processing

The Ni-rich L2 metal has higher contents of HRSE and MVSE than those predicted by the fraction crystallization sequence of the L1 metal with such high Ni contents (Figures 7–11). Since the silicates in L2 have a chondritic REE pattern (Ivanova et al., 2022), we suggest that the L2 metal could partially incorporate the primitive slightly Ni-rich metal from a chondritic body in the impact plume produced by the bodies in catastrophic collision. To obtain the observed shift from L1 metal trend (~6.4 wt% Ni at the Ir concentration as in L2, Figure 7a) to L2 metal (average 7.1 wt% Ni, Table 2) due

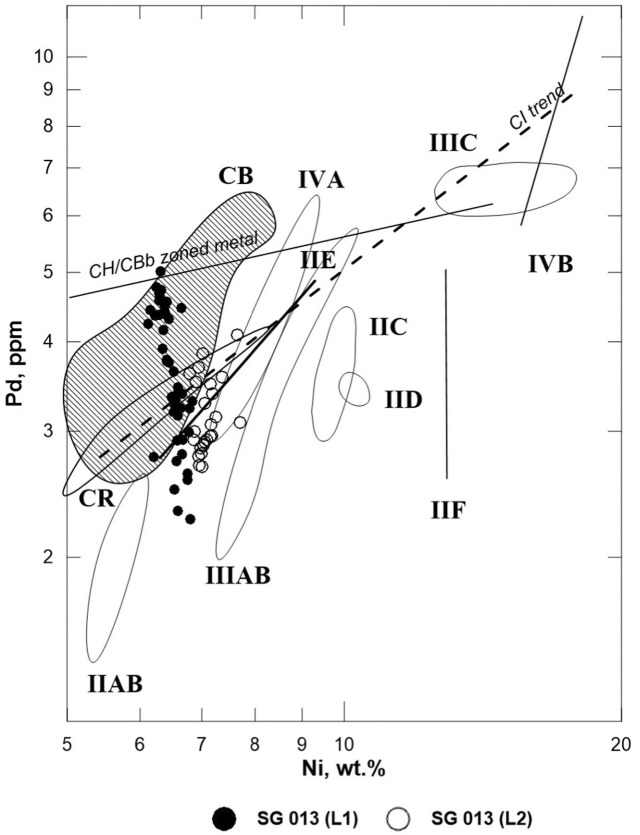

FIGURE 10. Pd-Ni distribution in the SG 013 metal of lithologies 1 (L1) and 2 (L2) compared to the metal composition from CR (Weyrauch et al., 2019), unzoned metal from CH, CB chondrites (shown as CB), trend of zoned metal from CH/CBb chondrites (Campbell et al., 2001, 2002; Weyrauch et al., 2019), metal from CI composition (Anders & Grevesse, 1989) and magmatic iron meteorites IC (Tornabene et al., 2023), IIAB, IIC, IID, IIIAB, IIIC, IVA (Scott, 1972), IIE (Wasson, 2017), IIF (Hilton et al., 2020), IVA (Wasson & Richardson, 2001), and IVB (Campbell & Humayun, 2005).

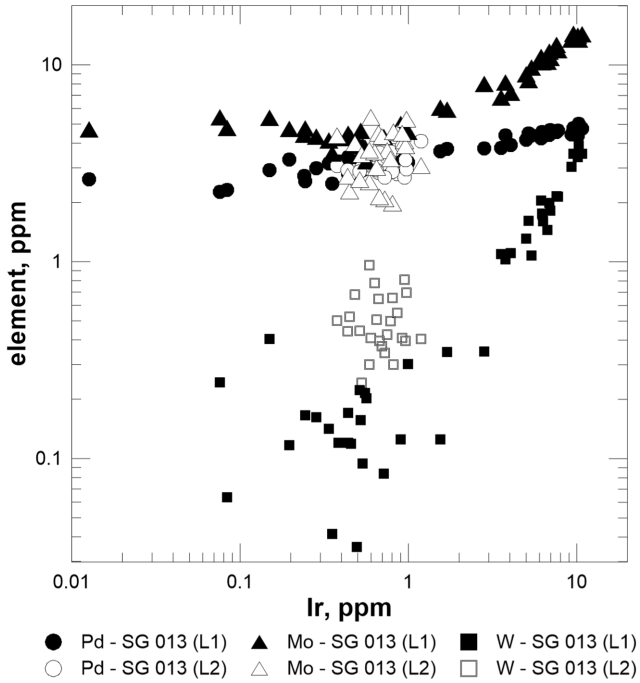

FIGURE 11. Correlations of W, Mo, and Pd with Ir in the SG 013 metal of lithologies 1 (L1) and 2 (L2).

to mixing the fractionated L1-like metal and chondrite metal in, for example, a 1:1 ratio (for simplification), the chondrite metal must contain 7.8% Ni. This concentration is higher than in CR but is in the CB metal range (Figure 7a) and seems to be realistic for this cosmochemical reservoir. The Ni-Ir plot (Figure 7a) shows that with a change in Ni by 1 wt%, the Ir concentration changes by ~1 ppm that is approximately the same as for SG 013 as for CR-CB metal compositions. Therefore, the Ir concentration in the metal mixture will change by about 0.5 ppm. With the Ir concentration range in L2 of 0.3–1 ppm, such a change is comparable with the absolute value of the relative error of the measurements of the standards with a most appropriate Ir concentration—North Chile Ir 2.49 ppm ±13% (Table S1). Thus, the mixing of the metal components mentioned above to form the L2 metal can result in observed Ni enrichment in L2 without detectable variations in Ir (and likely other HRSE) concentrations.

Compared to the compositions obtained by model fractional crystallization, the L2 metal is depleted in slightly varying Au, Cu, Ga, and it has extremely varying abundances of As and Sb (Figure 6). The observed behavior of these elements could result from nonequilibrium volatilization and recondensation in the impact plume, which changed the initially magmatic distribution of some medium and highly volatile elements. According to Weyrauch et al. (2019), Fe and Ni exhibited recondensation patterns for metal grains of CH-CBs in the plume. However, since the Fe/Pd ratio is not changed and the Fe/Au increases in both lithologies of SG 013, Fe could evaporate equally in both lithologies or could not evaporate, but Au was evaporated intensively in the L2 metal compared to the L1 metal (Figure 12a) because the L2 metal is more depleted in Au compared to the L1 metal (Figure 6a).

Metamorphism

Ivanova et al. (2022) showed that L2 was affected by thermal metamorphism up to 900°C. Observed enrichment of W in the L2 metal (Figure 11) can be caused by high temperature reduction of W from oxide of the host chondrite and diffusion redistribution of it to the metal. Such redox increase in W in chondritic metal is known in

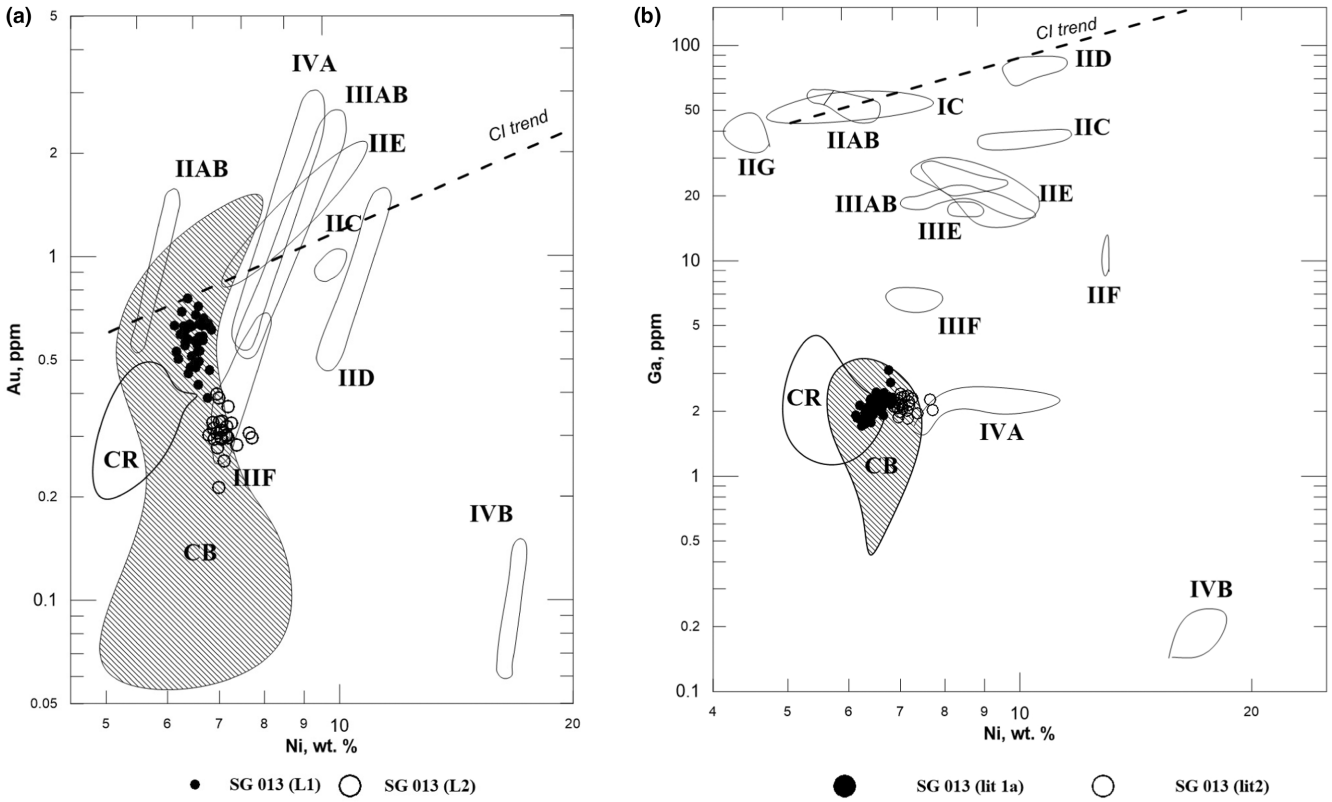

FIGURE 12. Au-Ni (a) and Ga-Ni (b) distributions in the SG 013 metal of lithologies 1 (L1) and 2 (L2) compared to the metal composition from CR (Kong et al., 1999; Kong & Palme, 1999), unzoned metal from CH, CB chondrites (shown as CB) and trend of zoned metal from CH/CBb chondrites (Campbell et al., 2001, 2002; Weyrauch et al., 2019), CI composition (Anders & Grevesse, 1989) and magmatic iron meteorites IC (Tornabene et al., 2023), IIAB (Wasson et al., 2007), IIIAB (Wasson, 1999), IIC, IID, IIIC (Scott, 1972; Scott & Wasson, 1975), IIE (Wasson, 2017), IIF (Hilton et al., 2020), IVA (Wasson & Richardson, 2001), and IVB (Campbell & Humayun, 2005).

ordinary chondrites (Humayun & Campbell, 2002) where the carbon like graphite or carbon-bearing presolar grains (Huss, 1990) can act as a reductant. If W was initially lithophile, metamorphic equilibration resulted in reduction of W and its transfer from nonmetallic phases to metal. The HRSE with exception of W were not affected by metamorphism because these chemical elements do not participate in metamorphic redox reactions. The mid-VSE and VSE, which many of them have affinities to sulfur also were not involved in the metamorphic exchanges due to general depletion of sulfur in SG 013.

Thus, the L2 metal composition most possibly originates from the same differentiated body as L1 metal during the same fractional crystallization of the metal melt, but in contrast to that, the L2 metal recorded traces of mixing of the fractionated metal with a primitive metal of the second colliding primitive body and was affected by unequilibrium evaporation of highly volatile elements in the plume and by high temperature metamorphic reactions that resulted in the reduction of W and redistribution of W into the L2 metal.

Genetic Relationship Between the Two Lithologies of SG 013

According to the generally accepted process of CB chondrite formation (Bollard et al., 2015; Fedkin et al., 2015; Ivanova et al., 2022; Krot et al., 2005, 2023; Oulton et al., 2016; Stewart et al., 2019a, 2019b), the chondrites were formed from an impact plume after a catastrophic collision of two different bodies. Based on the oxygen isotopic composition of CB chondrites (e.g., Krot et al., 2010), both bodies were CR-related. Fedkin et al. (2015) showed that if a CR chondrite body is differentiated into a core, a relatively CaO-, Al_2O_3-poor mantle, and a CaO-, Al_2O_3-rich crust, a collision between it and an identical body can produce the necessary chemical conditions for the condensation of CB chondrules. Oulton et al. (2016) also mentioned that variation in the LREE in the Gujba chondrules is essentially impossible to accomplish by processes involving vapor–liquid or vapor–solid exchange of REE and appears to have been inherited from a differentiated target. However, it was

not reported in publications about the magmatic signature of the metal composition of the Gujba and other CB chondrites' precursors. Probably, this signature was completely erased by the intensive plume processes in the Gujba metal, or their metal precursor was not differentiated. The siderophile element correlations in the CH and CBa-unzoned metal are absent, but the distribution of these elements in the CH and CBb-zoned metal indicates dependence on their volatility. Thus, it is unclear whether the precursor metal of other CB chondrites was differentiated or not.

Our results on SG 013 completely agree with this background. We showed that both of the colliding bodies were CR-like. One of the bodies was differentiated based on REE distribution in silicates of L1 lithology (Ivanova et al., 2022) and the fractionated composition of metal originates from the core of the differentiated body, suggesting that at the moment of collision, the differentiated body also had a silicate layer in addition to a metallic core. Other colliding bodies were primitive based on the chondritic distribution of REEs of the L2 silicates.

The trace element distribution of metal from the L1 and L2 lithologies suggests a range of fractional crystallization products of a differentiated metallic (Fe-Ni-S) liquid. Our model reproduces the L1 and L2 metal compositions better only when 13 wt% of sulfur is included in the metal core (Figure 6b–f). This high S content in the melt almost corresponds to the amount of S (12 wt%) in the fractional crystallization models calculated for the magmatic iron meteorites (e.g., Goldstein et al., 2009; Wasson, 1999). The Os/Ir < 1 in the L1 metal indicates its crystallization from sulfur-rich Fe,Ni melt as well (Chabot et al., 2003). The S abundance in CR chondrites is in the range 1.31–2.66 wt% (Weisberg et al., 1993). If all sulfur, nickel, and iron transferred into the Fe-Ni-S liquid, then the maximum S content in the melt will be 9.6 wt%. To get 13 wt% of S, the original CR-like chondrite composition should contain ~3.3 wt% of S. It is only 1.2 times more than that in CR chondrites. Due to the scarce data on bulk S content in CR chondrites, the precursor chondrite could contain more sulfur than that in known CR chondrites. Either the original Fe-Ni-S melt was locally enriched in sulfur as an immiscible liquid compared to the bulk melt (e.g., Chabot & Haack, 2006 and references therein). However, SG 013 is poor in sulfides and VSE. It could be explained by evaporation in the impact event and removal of S and VSE from the plume region where the SG 013 metal was processed.

The big metal globules from L1 contain a whole range of metal compositions formed during fractional crystallization, while the smaller globules contain only the HRSE-poor metal which is similar in composition to the L2 metal. We propose that possibly the HRSE-poor late fractions of metal crystallization were more dispersed during collision. The temperature in the plume, where the metal globules of L1 were formed, was not high enough for evaporation of HRSE for elements which are more refractory than Ni. Being together inside big metal globules of L1, compositions of different portions of metal were not equilibrated regarding highly refractory siderophile elements, possibly due to a quick cooling that preserved the initial magmatic distribution pattern.

Distribution of HRSE in the L1 metal has a different pattern than that of CB-CH metal having flat distribution of HRSE with negative anomalies of W and Mo which are typical for condensation process in the plume in oxidizing conditions (Weyrauch et al., 2019). According to Weyrauch et al. (2019) W and Mo should have a negative anomaly compared to other RSE, since these elements are oxygen very sensitive. An impact of planetesimals is likely to form a vapor plume with highly oxidizing conditions (with enhanced dust/gas ratios), higher than in the canonical solar nebula. Mo is more oxygen sensitive than W during condensation and is expected to be stronger depleted than W. On the other hand, W is more oxygen sensitive than Mo during evaporation. In the case of the SG 013 metal, we did not observe W and Mo negative anomalies among other HRSE since Wo and Mo are distributed into the solid phase according to crystallization sequence in reduced environment. Therefore, in contrast to the CB-CH metal, the L1 HRSEs (including W and Mo) were not affected by condensation–evaporation process in the plume, since the oxygen pressure in this plume region must have been below the W-WO_2 buffer.

During this catastrophic impact event when the metallic core of the parent body was disrupted, mixing of solid and molten metal particles of different compositions produced the metal globules from L1. This is consistent with the conclusions of Lorenz et al. (2023) that the metal globules from L1 were aggregates of smaller solid or molten metal grains which were combined with each other, similar to that in other CB chondrites (Florin et al., 2021; Weisberg et al., 2001; Weyrauch et al., 2019).

We propose that after a catastrophic impact event, the L1 and L2 materials were moved in various directions depending on the disruption process of the collided bodies, dynamics of ejecta, impact plume expansion, and gravitational interactions of the postimpact remnants of the bodies. Metal particles representing different products of fractional crystallization were aggregated together in the vapor plume, forming the L1 globules, and mixed with silicate material originating from a differentiated body forming the L1 lithology. The part of the metal representing HRSE-poor fractions of the differentiated body core was ejected to the plume region enriched in disruption products of the second primitive impactor, mixed with its primitive metal and silicates, and formed the L2 lithology.

Then, during re-accretion, the L1 and L2 materials were deposited in different parts of the newly formed body. L1 was deposited near the surface, cooled quickly and suffered impact metamorphism. Occasionally, the L2 material could be buried deeper in the body and was cooled more slowly than L1 to be affected by thermal metamorphism leading to silicate recrystallization, kamacite and taenite formation and to W re-distribution to the metal. It remains unclear whether all CB chondrites were formed by a single common catastrophic event, or whether at least anomalous CB chondrites like SG 013 and Fountain Hills are the result of separate impact events.

SUMMARY

The SG 013 chondrite is formed from CR-like precursors and its characteristics correspond to the formation of CB chondrites in the impact plume by the catastrophic collision of differentiated and primitive bodies. However, the SG 013 chondrite is unique among other CB chondrites, since it preserved the fractionated magmatic REE patterns of a silicate shell of a differentiated parent body in L1 together with the primitive silicate composition of L2 (Ivanova et al., 2022).

The composition of the metal globules of lithology 1 and metal particles of lithology 2 is distinct from that of typical CB chondrites and zoned metal from CH/CBb chondrites. Although the metals from both lithologies are in the range of CB chondrites in Ni and Co, the Ni and Co distribution in the L1 metal is similar in configuration to some magmatic irons, in contrast to the Ni and Co distribution in the L2 metal which is not correlated. The Ni content in L2 is higher than that of L1, probably due to the addition of metal with higher Ni to the common metal precursor for the L1 and L2 metals. Both lithologies are depleted in Cr like the irons of IIAB, IIIAB, and IVAB groups in comparison with the CH-CB metal.

Compositions of the L1 metal particles are fractionated and show enriched as well as depleted patterns of highly refractory siderophile elements (W, Re, Os, Ir, Pt, Ru, Rh, and Mo) relative to CI composition. The L1 metal is depleted in Au and in volatile siderophile elements (VSE) such as Sb, As, and Ga relative to CI composition. The L2 metal is strongly depleted in HRSE and VSE, similar to the HRSE-poor compositions of the L1 metal, and the L2 metal is also depleted in Pd and Au relative to the CI composition. The primary igneous signature of the L1 metal was overprinted to some extent by high temperature plume processing.

Likely, the L1 metal represents a full range of fraction crystallization products in a parent body core. The L2 metal is depleted in HRSE similar to some L1 metals and could represent only a portion of fractionated metal co-genetic to L1 metal mixed with the primitive metal from the chondritic colliding body. The molten core material was recombined in the impact plume with differentiated silicates forming L1, while a portion of HRSE-poor metal was mixed with the chondritic metal and silicates producing L2.

The model of fractional crystallization of the CR-like metal reproduces the siderophile elements distribution in L1 and L2 compositions with addition of 13% of sulfur to the metal melt. The sulfide-poor SG 013 composition is explained by evaporation of S in the impact plume. The HRSE-poor late products of fraction crystallization acquired a mid-VSE-, and VSE-depleted pattern due to evaporation in the plume.

After re-accretion of the L2 from the plume, the L2 metal was affected by solid-state thermal metamorphism in the newly formed parent body, resulting in the redistribution of W between metal and silicates due to the redox reactions.

Acknowledgments—The work was carried out within the state assignment of the Vernadsky Institute of Geochemistry and Analytical Chemistry of the Russian Academy of Sciences (GEOHI RAS). Laser ablation analysis at FSU was supported by grants from the National Aeronautics and Space Administration. A portion of this work was performed at the National High Magnetic Field Laboratory, which is supported by the National Science Foundation Cooperative Agreement No. DMR-1644779 and the state of Florida. The authors thank the Associate Editor, Y. Marrocchi, the reviewer, E. van Kooten, and two anonymous reviewers for their fruitful comments and suggestions which help to significantly improve the paper.

Data Availability Statement—Data available on request from the authors.

Editorial Handling—Dr. Yves Marrocchi

REFERENCES

Anders, E., and Grevesse, N. 1989. Abundances of the Elements: Meteoritic and Solar. *Geochimica et Cosmochimica Acta* 53: 197–214.

Bollard, J., Connelly, J., and Bizzarro, M. 2015. Pb-Pb Dating of Individual Chondrules from the CBa Chondrite Gujba: Assessment of the Impact Plume Formation Model. *Meteoritics & Planetary Science* 50: 1197–1216.

Campbell, A. J., and Humayun, M. 1999. Trace Element Microanalysis in Iron Meteorites by Laser Ablation ICPMS. *Analytical Chemistry* 71: 939–946.

Campbell, A. J., and Humayun, M. 2005. Compositions of Group IVB Iron Meteorites and their Parent Melt. *Geochimica et Cosmochimica Acta* 69: 4733–44.

Campbell, A. J., Humayun, M., Krot, A., and Keil, K. 2001. Origin of Zoned Metal Grains in the QUE 94411 Chondrite. *Geochimica et Cosmochimica Acta* 65: 163–180.

Campbell, A. J., Humayun, M., and Weisberg, M. K. 2002. Siderophile Element Constraints on the Formation of Metal in the Metal-Rich Chondrites Bencubbin, Gujba and Weatherford. *Geochimica et Cosmochimica Acta* 66: 647–660.

Campbell, A. J., Humayun, M., and Weisberg, M. K. 2005. Compositions of Unzoned and Zoned Metal in the CBb Chondrites Hammadah al Hamra 237 and Queen Alexandra Range 94627. *Meteoritics & Planetary Science* 40: 1131–48.

Chabot, N. J., and Drake, M. J. 2000. Crystallization of Magmatic Iron Meteorites: The Effects of Phosphorus and Liquid Immiscibility. *Meteoritics & Planetary Science* 35: 807–816.

Chabot, N. L., Campbell, A. J., Jones, J. H., Humayun, M., and Agee, C. B. 2003. An Experimental Test of Henry's Law in Solid Metal Liquid Metal Systems with Implications for Iron Meteorites. *Meteoritics & Planetary Science* 38: 181–196.

Chabot, N. L., Campbell, A. J., Jones, J. H., Humayun, M., and Lauer, H. V., Jr. 2006. The Influence of Carbon on Trace Element Partitioning Behavior. *Geochimica et Cosmochimica Acta* 70: 1322–35.

Chabot, N. L., and Haack, H. 2006. Evolution of Asteroidal Cores. In *Meteorites and the Early Solar System II*, edited by D. S. Lauretta, and H. Y. McSween, Jr., 747–771. Tucson, AZ: University of Arizona Press.

Chabot, N. L., and Jones, J. H. 2003. The Parameterization of Solid Metal-Liquid Metal Partitioning of Siderophile Elements. *Meteoritics & Planetary Science* 38: 1425–36.

Chabot, N. L., Saslow, S. A., McDonough, W. F., and Jones, J. H. 2009. An Investigation of the Behavior of Cu and Cr during Iron Meteorite Crystallization. *Meteoritics & Planetary Science* 44: 505–519.

Connelly, J. N., Bizzarro, M., Krot, A. N., Nordlunds, A., Wielandt, D., and Ivanova, M. A. 2012. The Absolute Chronology and Thermal Processing of Solids in the Solar Protoplanetary Disk. *Science* 338: 651–55.

Corrigan, C. M., Chabot, N. L., McCoy, T. J., McDonough, W. F., Watson, H. C., Saslow, S. A., and Ash, R. D. 2009. The Iron–Nickel–Phosphorus System: Effects on the Distribution of Trace Elements during the Evolution of Iron Meteorites. *Geochimica et Cosmochimica Acta* 73: 2674–91.

Fedkin, A. V., Grossman, L., Humayun, M., Simon, S. B., and Campbell, A. J. 2015. Condensates from Vapor Made by Impacts between Metal-, Silicate-Rich Bodies: Comparison with Metal and Chondrules in CB Chondrites. *Geochimica et Cosmochimica Acta* 164: 236–261.

Florin, G., Luais, B., Alard, O., and Rushmer, T. 2021. Condensation and Evaporation Processes during CB Chondrite Formation: Insights from Ge Isotopes and Highly Siderophile Element Abundances. *Meteoritics & Planetary Science* 56: 1191–1211.

Goldstein, J. I., Scott, E. R. D., and Shabot, N. L. 2009. Iron Meteorites: Crystallization, Thermal History, Parent Bodies, and Origin. *Chemie der Erde* 69: 293–325.

Haack, H., and Scott, E. R. D. 1992. Asteroid Core Crystallization by Inward Dendritic Growth. *Journal of Geophysical Research* 97(E9): 14727–34.

Hilton, C. D., Ash, R. D., and Walker, R. J. 2020. Crystallization Histories of the Group IIF Iron Meteorites and Eagle Station Pallasites. *Meteoritics & Planetary Science* 55: 2570–86.

Hoffman, V. 2021. *Chemical and Petrological Characterization of the Unique CBa Chondrite Sierra Gorda 013*. Master Thesis. Frankfurt am Mein: Institute of Geoscience, Department of Mineralogy, Goethe Universität.

Humayun, M. 2012. Chondrule Cooling Rates Inferred from Diffusive Profiles in Metal Lumps in the Acfer 097 CR2 Chondrite. *Meteoritics & Planetary Science* 47: 1191–1208.

Humayun, M., and Campbell, A. J. 2002. The Duration of Ordinary Chondrite Metamorphism Inferred from Tungsten Microdistribution in Metal. *Earth and Planetary Science Letters* 198: 225–243.

Huss, G. R. 1990. Ubiquitous Interstellar Diamond and SiC in Primitive Chondrites: Abundances Reflect Metamorphism. *Nature* 347: 159–162.

Ivanova, M. A., Kononkova, N. N., Krot, A. N., Greenwood, R. C., Franchi, I. A., Verchovsky, A. B., Trieloff, M., Korochansteva, E. V., and Brandstaetter, F. 2008. The Isheyevo Meteorite: Mineralogy, Petrology, Bulk Chemistry, Oxygen, Nitrogen, Carbom Isotopic Compositions and ^{40}Ar-^{39}Ar Ages. *Meteoritics & Planetary Science* 43: 915–940.

Ivanova, M. A., Lorenz, C. A., Humayun, M., Yang, S., Ma, C., Teplyakova, S. N., Franchi, I. A., and Korochantsev, A. V. 2022. Sierra Gorda 013: Unusual CBa-Like Metal-Rich Chondrite. *Meteoritics & Planetary Science* 57: 657–682.

Ivanova, M. A., Ma, C., Lorenz, C. A., Franchi, I. A., and Kononkova, N. N. 2019. A New Unusual Bencubbinite (CBa), Sierra Gorda 013, and its Unique V-Rich Sulfides. *Meteoritics & Planetary Science* 54: A.185.

Jochum, K. P., Jochum, K. P., Stoll, B., Herwig, K., Willbold, M., Hofmann, A. W., Amini, M., et al. 2006. MPI-DING Reference Glasses for In Situ Microanalysis: New Reference Values for Element Concentrations and Isotope Ratios. *Geochemistry, Geophysics, Geosystems* 7: 1–44.

Jones, J. H., and Drake, M. J. 1983. Experimental Investigations of Trace Element Fractionation in Iron Meteorites, II: The Influence of Sulfur. *Geochimica et Cosmochimica Acta* 47: 1199–1209.

Kallemeyn, G. W., Boynton, W. V., Willis, J., and Wasson, J. T. 1978. Formation of Bencubbin Polymict Meteoritic Breccia. *Geochimica et Cosmochimica Acta* 42: 507–515.

Koefoed, P., Pravdivtseva, O., Ogliore, R., Jiang, Y., Lodders, K., Neuman, M., and Wang, K. 2022. The Dynamic Formation Process of the CB Chondrite Gujba. *Geochimica et Cosmochimica Acta* 332: 33–56.

Kong, P., Ebihara, M., and Palme, H. 1999. Distribution of Siderophile Elements in CR Chondrites: Evidence for Evaporation and Recondensation during Chondrule Formation. *Geochimica et Cosmochimica Acta* 63: 2637–52.

Kong, P., and Palme, H. 1999. Compositional and Genetic Relationship between Chondrules, Chondrule Rims, Metal, and Matrix in the Renazzo Chondrite. *Geochimica et Cosmochimica Acta* 63: 3673–82.

Krot, A. N., Amelin, Y., Cassen, P., and Meibom, A. 2005. Young Chondrules in CB Chondrites from a Giant Impact in the Early Solar System. *Nature* 436: 989–992.

Krot, A. N., Meibom, A., Weisberg, M. K., and Keil, K. 2002. The CR Chondrite Clan: Implications for Early

Solar System Processes. *Meteoritics & Planetary Science* 37: 1451–90.

Krot, A. N., Nagashima, K., and Petaev, M. I. 2012. Isotopically Uniform, 16O-depleted Calcium, Aluminum-Rich Inclusions in CH and CB Carbonaceous Chondrites. *Geochimica et Cosmochimica Acta* 83: 159–178.

Krot, A. N., Nagashima, K., Bizzarro, M., Huss, G. R., Davis, A. M., McKeegan, K. D., Meyer, B. S., and Ulyanov, A. A. 2008. Multiple Generations of Refractory Inclusions in the Metal-Rich Carbonaceous Chondrites Acfer 182/214 and Isheyevo. *The Astrophysical Journal* 672: 713–721.

Krot, A. N., Nagashima, K., Ivanova, M. A., Lauretta, D., Libourel, G., Brandon, C., Johnson, B. C., et al. 2023. Oxygen Isotopic Compositions of Chondritic and Achondritic Lithologies in the Anomalous CB Carbonaceous Chondrites Sierra Gorda 013 and Fountain Hills. *Meteoritics & Planetary Science* 58: in press.

Krot, A. N., Nagashima, K., Yoshitake, M., and Yurimoto, H. 2010. Oxygen Isotopic Compositions of Chondrules from the Metal-Rich Chondrites Isheyevo (CH/CBb), MAC 02675 (CBb) and QUE 94627 (CBb). *Geochimica et Cosmochimica Acta* 74: 2190–2211.

Krot, A. N., Petaev, M. I., Nagashima, K., Dobrica, E., Johnson, B. C., and Cashion, M. D. 2022. Impact Plume-Formed and Protoplanetary Disk High-Temperature Components in CB and CH Metal-Rich Carbonaceous Chondrites. *Meteoritics & Planetary Science* 57: 352–380.

Lauretta, D. S., Goreva, J. S., Hill, D. H., Killgore, M., La Blue, A. R., Campbell, A., Greenwood, R. C., Franchi, I. A., and Verchovsky, A. B. 2009. The Fountain Hills Unique CB Chondrite: Insights into Thermal Processes on the CB Parent Body. *Meteoritics & Planetary Science* 44: 823–838.

Lauretta, D. S., Killgore, M., Greenwood, R. C., Verchovsky, A. B., and Franchi, I. A. 2004. The Fountain Hills meteorite: A new CBa chondrite from Arizona. In *35th Lunar and Planetary Science Conference*. Abstract #1255.

Lorenz, C. A., Ivanova, M. A., Zinovieva, N. G., Ryazantsev, K. M., and Korochantsev, A. V. 2023. Heterogeneity of Planetesimal Collisional Plime Probed by Glass Inclusions in Metal Globules of Sierra Gorda 013, Unusual CBa-Like Chondrite. *Meteoritics & Planetary Science* 58: 241–258.

Meibom, A., Petaev, M. I., Krot, A. N., Wood, J. A., and Keil, K. 1999. Primitive Fe,Ni Metal Grains in CH Carbonaceous Chondrites Formed by Condensation from a Gas of Solar Composition. *Journal of Geophysical Research* 104: 22053–59.

Newsom, H. E., and Drake, M. J. 1979. The Origin of Metal Clasts in the Bencubbin Meteorite Breccia. *Geochimica et Cosmochimica Acta* 43: 689–707.

Oulton, J., Humayun, M., Fedkin, A., and Grossman, L. 2016. Chemical Evidence for Differentiation, Evaporation and Recondensation from Silicate Clasts in Gujba. *Geochimica et Cosmochimica Acta* 177: 254–274.

Petaev, M. I., Meibom, A., Krot, A. N., Wood, J. A., and Keil, K. 2001. The Condensation Origin of Zoned Metal Grains in Queen Alexandra Range 94411: Implications for the Formation of the Bencubbin-Like Chondrites. *Meteoritics & Planetary Science* 36: 93–106.

Ryan, D. E., Holzbecher, J., and Brooks, R. R. 1990. Rhodium and Osmium in Iron Meteorites. *Chemical Geology* 85: 295–303.

Scott, E. R. D. 1972. Chemical Fractionation in Iron Meteorites and its Interpretation. *Geochimica et Cosmochimica Acta* 36: 1205–36.

Scott, E. R. D., and Wasson, J. T. 1975. Classification and Properties of Iron Meteorites. *Reviews of Geophysics* 13: 527–546.

Stewart, S. T., Carter, P. J., Davies, E. J., Lock, S. J., Kraus, R. G., Root, S., Petaev, M. I., and Jacobsen, S. B. 2019a. Impact Vapor Plume Expansion and Hydrodynamic Collapse in the Solar Nebula. *50th Lunar and Planetary Science Conference*, abstract #1250.

Stewart, S. T., Carter, P. J., Davies, E. J., Lock, S. J., Kraus, R. G., Root, S., Petaev, M. I., and Jacobsen, S. B. 2019b. Collapsing Impact Vapor Plume Model for Chondrule and Chondrite Formation. *50th Lunar and Planetary Science Conference*, abstract #1251.

Teplyakova, S. N., Humayun, M., Lorenz, C. A., and Ivanova, M. A. 2022. Geochemical Evidence of the IIE Parent Body Origin from the H Chondrite Material. *Meteoritics & Planetary Science* 57: 1745–58.

Tornabene, H. A., Ash, R. D., Walker, R. J., and Bermingham, K. R. 2023. Genetics, Age, and Crystallization History of Group IC Iron Meteorites. *Geochimica et Cosmochimica Acta* 340: 108–119.

Van Kooten, E. M. M. E., Kubik, E., Siebert, J., Heredia, B. D., Thomsen, T. B., and Moynier, F. 2022. Metal Compositions of Carbonaceous Chondrites. *Geochimica et Cosmochimica Acta* 321: 52–77.

Van Kooten, E. M. M. E., Wielandt, D., Schiller, M., Nagashima, K., Thomen, A., Larsen, K. K., Olsen, M. B., Nordlund, A., Krot, A. N., and Bizzarro, M. 2016. Isotopic Evidence for Primordial Molecular Cloud Material in Metal-Rich Carbonaceous Chondrites. *Proceedings of the National Academy of Sciences of the United States of America* 113: 2011–16.

Walker, R. J., McDonough, W. F., Honesto, J., Chabot, N. L., McCoy, T. J., Ash, R. D., and Bellucci, J. J. 2008. Modeling Fractional Crystallization of Group IVB Iron Meteorites. *Geochimica et Cosmochimica Acta* 72: 2198–2216.

Wasson, J. T. 1999. Trapped Melt in IIIAB Irons; Solid/Liquid Elemental Partitioning during the Fractionation of the IIIAB Magma. *Geochimica et Cosmochimica Acta* 63: 2875–89.

Wasson, J. T. 2017. Formation of Non-magmatic Iron-Meteorite Group IIE. *Geochimica et Cosmochimica Acta* 197: 396–416.

Wasson, J. T., and Choe, W.-H. 2009. The IIG iron meteorites: Probable formation in the IIAB core. *Geochimica et Cosmochimica Acta* 73: 4879–90.

Wasson, J. T., and Choi, B.-G. 2003. Main-Group Pallasites: Chemical Composition, Relationship to IIIAB Irons, and Origin. *Geochimica et Cosmochimica Acta* 67: 3079–96.

Wasson, J. T., Huber, H., and Malvin, D. J. 2007. Formation of IIAB Iron Meteorites. *Geochimica et Cosmochimica Acta* 71: 760–781.

Wasson, J. T., and Kallemeyn, G. W. 1990. Allan Hills 85085: A Subchondritic Meteorite of Mixed Nebular and Regolithic Heritage. *Earth and Planetary Science Letters* 101: 148–161.

Wasson, J. T., and Rubin, A. E. 2010. Metal in CR Chondrites. *Geochimica et Cosmochimica Acta* 74: 2212–30.

Wasson, J. T., Ouyang, X., Wang, J., and Jerde, E. 1989. Chemical Classification of Iron Meteorites: XI. Multi Element Studies of 38 New Irons and the High Abundance of Ungrouped Irons from Antarctica. *Geochimica et Cosmochimica Acta* 53: 735–744.

Wasson, J. T., and Richardson, J. W. 2001. Fractionation Trends among IVA Iron Meteorites: Contrasts with IIIAB Trends. *Geochimica et Cosmochimica Acta* 65: 951–970.

Weisberg, M. K., and Ebel, D. S. 2009. The Fountain Hills Impact-Modified CB Chondrite Thermal History of the CB Asteroid. *Meteoritics & Planetary Science* 44: 201–210.

Weisberg, M. K., and Kimura, M. 2010. Petrology and Raman Spectroscopy of High Pressure Phases in the Gujba CB Chondrite and the Shock History of the CB Parent Body. *Meteoritics & Planetary Science* 45: 873–884.

Weisberg, M. K., Prinz, M., Clayton, R. N., and Mayeda, T. K. 1993. The CR (Renazzo-Type) Carbonaceous Chondrite Group and its Implications. *Geochimica et Cosmochimica Acta* 57: 1567–1686.

Weisberg, M. K., Prinz, M., Clayton, R. N., Mayeda, T. K., Grady, M. M., and Pillinger, C. T. 1995. The CR Chondrite Clan. *Proceedings of NIPR Symposium on Antarctic Meteorites* 8: 11–32.

SUPPORTING INFORMATION

Additional supporting information may be found in the online version of this article.

Weisberg, M. K., Prinz, M., Clayton, R. N., Mayeda, T. K., Sugiura, N., Zashu, S., and Ebihara, M. 2001. A New Metal-Rich Chondrite Grouplet. *Meteoritics & Planetary Science* 36: 401–418.

Weisberg, M. K., Prinz, M., and Nehru, C. E. 1990. The Bencubbin Chondrite Breccia and its Relationship to CR Chondrites and the ALH85085 Chondrite. *Meteoritics* 25: 269–279.

Weyrauch, M., Zipfel, J., and Weyer, S. 2019. Origin of Metal from CB Chondrites in an Impact Plume - A Combined Study of Fe and Ni Isotope Composition and Trace Element Abundances. *Geochimica et Cosmochimica Acta* 246: 123–137.

Weyrauch, M., Zipfel, J., and Weyer, S. 2021. The Relationship of CH, CB, and CR Chondrites: Constraints from Trace Elements and Fe-Ni Isotope Systematics in Metal. *Geochimica et Cosmochimica Acta* 308: 291–309.

Wölfer, E., Budde, G., and Kleine, T. 2023. Age and Genetic Relationships among CB, CH and CR Chondrites. *Earth and Planetary Astrophysics* (astro-ph.EP): arXiv:2310.12749v1.

Yang, S., Humayun, M., and Salters, V. J. M. 2018. Elemental Systematics in MORB Glasses from the Mid-Atlantic Ridge. *Geochemistry, Geophysics, Geosystems* 19: 4236–59. https://doi.org/10.1029/2018GC007593.

Table S1. Measurements of the metal standards for the LA-ICP-MS analysis.